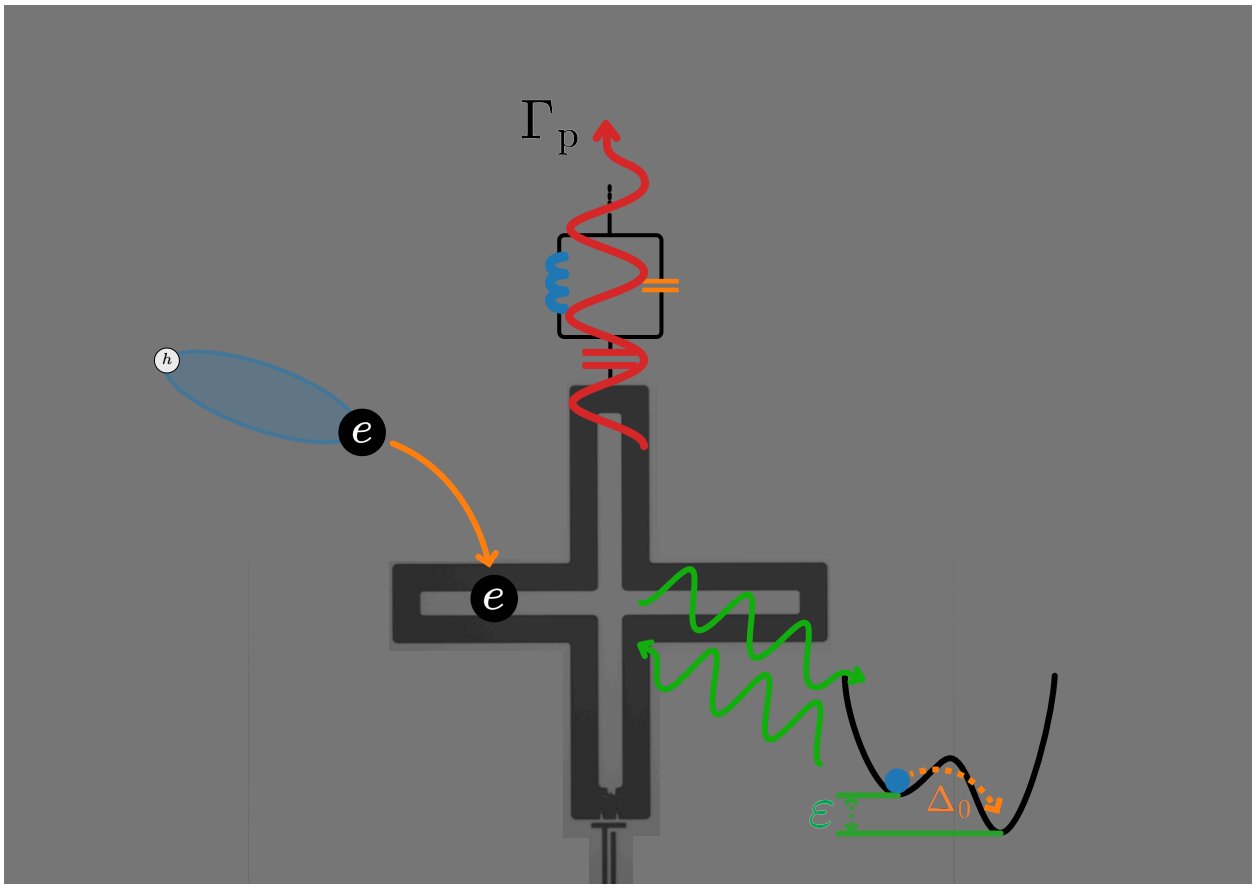

Benchmarking the design, fabrication and shielding of superconducting qubits

Measurements of environmental effects in transmons

Master's thesis in Nanotechnology

HALLDÓR JAKOBSSON

DEPARTMENT OF MICROTECHNOLOGY AND NANOSCIENCE
CHALMERS UNIVERSITY OF TECHNOLOGY
Gothenburg, Sweden 2024
www.chalmers.se

Master's thesis 2024

Benchmarking the design, fabrication and shielding of superconducting qubits

Measurements of environmental effects in transmons

HALLDÓR JAKOBSSON

CHALMERS
UNIVERSITY OF TECHNOLOGY

Department of Microtechnology and Nanoscience
Quantum Technology
Quantum Technology Laboratory
Chalmers University of Technology
Gothenburg, Sweden 2024

Benchmarking the design, fabrication and shielding of superconducting qubits
Measurements of environmental effects in transmons
HALLDÓR JAKOBSSON

Supervisor: Giovanna Tancredi, Microtechnology and Nanoscience
Co-supervisor: Amr Osman, Microtechnology and Nanoscience
Examiner: Jonas Bylander, Microtechnology and Nanoscience

Master's Thesis 2024
Department of Microtechnology and Nanoscience
Quantum Technology
Quantum Technology Laboratory
Chalmers University of Technology
SE-412 96 Gothenburg
Telephone +46 31 772 1000

Cover: Micrograph of superconducting qubit pad. Components of the environment, with which the qubit interacts with, have been schematically drawn on top of the micrograph.

Typeset in LaTeX
Printed by Chalmers Reproservice
Gothenburg, Sweden 2024

Benchmarking the design, fabrication and shielding of superconducting qubits
Measurements of environmental effects in transmons
HALLDÓR JAKOBSSON
Department of Microtechnology and Nanoscience
Chalmers University of Technology

Abstract

Superconducting qubits interact with their environment, which inherently limits their coherence. In this thesis, we describe measurements and present experimental results for characterising the qubits interaction with its environment. We performed flux pulse distortion measurements which allowed us to correct the flux pulse with 0.2% error of the target pulse. A two-level-system (TLS) defect spectroscopy measurement showed a TLS density of 14 ± 2 TLS/GHz, with TLS-qubit coupling between 50 kHz and 650 kHz, and TLS lifetime less than 200 ns. Repeating the TLS spectroscopy measurement every hour for twelve hours showed TLS drifting and telegraphic switching between frequencies with a timescale on the order of hours. Using a parity selective Ramsey sequence, we measured the qubit parity switching rate due to quasiparticles (QPs) as 500 ± 100 Hz, which randomly varied between 200 Hz to 800 Hz over 24 hours. We designed and measured a device where the qubit frequency could be tuned through the resonator. To this end, we measured the qubit decay rate as a function of frequency and found the single mode Purcell approximation to be negligible compared to TLS and QP losses in this device. In addition, the TLS loss was measured as $F\delta_{\mathrm{TLS}} = (3 \pm 1) \cdot 10^{-6}$, and the quasiparticle density normalised to the density of Cooper pairs as $x_{\mathrm{QP}} = (6 \pm 1) \cdot 10^{-7}$. In equilibrium, this quasiparticle density would corresponds to a qubit temperature of 147 ± 2 mK, since the qubit is cooled down to 10 mK, we interpret this as the presence of non-equilibrium quasiparticles.

Keywords: Quantum, superconductor, transmon, TLS, quasiparticle, Purcell, defect, experiment, distortion, flux.

Acknowledgements

This thesis is dedicated to my parents, Jakob Ragnarsson and Margrét Dögg Halldórsdóttir. Thank you for always supporting me.

Halldór Jakobsson, Gothenburg, 4th of July, 2024

List of Acronyms

Below is the list of acronyms that have been used throughout this thesis listed in alphabetical order:

AWG	Arbitrary waveform generator
CPW	Coplanar waveguide
CQED	Circuit quantum electrodynamics
FIR	Finite impulse response
HMM	Hidden Markov Model
HP	High-pass
IIR	Infinite impulse response
JJ	Josephson junction
LNA	Low-noise amplifier
LO	Local oscillator
LP	Low-pass
PICT	Patch-integrated cross-type
QP	Quasiparticle
RO	Readout
SIS	Superconductor-insulator-superconductor
SQUID	Superconducting quantum interference device
TLS	Two-level-system

Nomenclature

Below is the nomenclature of indices, sets, parameters, and variables that have been used throughout this thesis.

Indices

i, j	Summation index, general index
n	Index of discrete function
sc	Superconductor
01	Ground-excited
QP	Quasiparticle
TLS	Two-level-system

Constants

Φ_0	Superconducting magnetic flux quantum	$h/2e \approx 2.0678 \cdot 10^{-15}$ Wb
h	Planck constant	$\approx 6.6261 \cdot 10^{-34}$ J Hz^{-1}
$\hbar$	Reduced Planck constant	$h/2\pi \approx 1.0546 \cdot 10^{-34}$ Js
e	Electron charge	$\approx 1.6022 \cdot 10^{-19}$ C
k_B	Boltzmann constant	$\approx 8.6173 \cdot 10^{-5}$ eV K^{-1}

Parameters

E_J	Josephson energy
I_C	Critical current
L_i	Inductance of i-th element
C_i	Capacitance of i-th element

E_C	Capacitive charging energy
ω_i	Angular frequency of i-th element
f_i	Frequency of i-th element
d	Asymmetry parameter
Φ	Magnetic flux
$\sigma_{x,y,z}$	Pauli matrices
$\sigma_{\pm}$	Pauli raising and lowering operators
H	Hamiltonian
S	Schrieffer-Wolff transformation operator
Δ	Generally difference between something. With a subscript, this is also used as a gap or tunnelling strength
$a^{(\dagger)}$	Annihilation (creation) operator
χ	Dispersive shift
S_{ij}	S matrix element
Q_e	External quality factor
Q_i	Internal quality factor
Q	Quality factor
η	Anharmonicity
a_i	Transfer function i-th amplitude
τ_i	Transfer function i-th timescale
Δ_0	Tunnelling strength between TLS states
$\mathcal{E}$	Energy difference between TLS states
E	Energy
Γ_i	Decay rate of i-th element
g	Coupling strength
$\lvert\cdot\rangle$	Ket
λ_n	n-th eigenvalue
c_n	n-th coefficient in linear combination
k_F	Fermi level
T	Temperature
Δ_{sc}	Superconducting gap
κ	Linewidth
$\mathcal{V}_i$	Measured i-th voltage value
$\langle\cdot\rangle$	Average
T_1	Qubit relaxation time

X_θ, Y_θ, Z_θ	Rotation around the X, Y and Z axis on the Bloch sphere by θ
φ	Phase
P	Parity
N	Number of records
F	Filling factor
δ	Loss tangent
x_{QP}	Ratio of broken Cooper pairs
A, B, C, D	General fitting parameters. Used in different context
γ	Coupling between feedline and resonator

Variables

t	Time
s	Laplace frequency
n	Discrete sampling index
z	Discrete Laplace frequency
V	Voltage

Contents

List of Figures

List of Tables

1
Introduction

Quantum computing has been shown to, theoretically, have the ability of solving computational tasks faster than classically possible [1]. Extremely simply put, this is due to the principles of quantum mechanics; superposition and entanglement [2]. There are many ways of physically implementing a quantum computer [3]. A promising quantum computing architecture is based on superconducting circuits [4, 5], due to the qubits strong coupling to microwaves and standard fabrication procedures [6, 7].

To manipulate and measure superconducting qubits, it is necessary to couple them to an environment which we control. This environment interacts with the qubit, allowing us to measure it, but negatively affects its coherence as well [8]. Once the qubit's door to the environment has been opened, the qubit can also interact with an uncontrollable environment, such as defects around the qubit [9], or residual excitations of the superconducting state [10]. To benchmark a qubit's operation and gain intuitive understanding for why some qubits perform better than others, we should measure the qubit's performance while also keeping track of how it interacts with its environment.

The aim of this thesis is to present measurement techniques for analysing some of the components of the environment that interact with our qubits, and discuss deviation from idealities. The thesis is organised as follows: in Chapter 2, we give a theoretical overview. This overview includes basic principles of superconducting qubits and how they are measured, covering also environmental effects such as two-level-system defects, quasiparticles and the Purcell effect. In Chapter 3, we discuss the practical aspects of the project, beginning with the experimental setup for qubit measurements, a description of the measured devices and their design, and later describing in detail the exact experiments used to measure how all the different environmental components affect the qubit. In Chapter 4, we present the results of the measurements and compare them with results found in literature and similar work. Finally, we conclude the thesis with Chapter 5, in which we discuss what was achieved in this project and what its results imply, or can be used for. We also mention how some of the experiments can be improved, and suggest future directions that can be pursued.

2
Theory

In this chapter we present the theory relevant to this project. We start by presenting the basic principles of superconducting qubits, with a focus on transmons. The flux tunable transmon's frequency can be varied by applying square pulses, which leads us into a discussion about pulse distortions and how they can be corrected. We then present some theoretical aspects of two-level-system defects and quasiparticles, i.e. the *evil* environment, before discussing briefly the Purcell effect.

2.1 The transmon

For quantum computing we need a computational basis, called a quantum bit (qubit), which mirrors the classical bit of zeros and ones. We also require the ability to drive transitions between the two basis states; this means that we can not use harmonic oscillators as qubits since all the energy levels are equidistant and we would not be able to prevent the qubit from being driven to arbitrarily high excitations.[1] Instead, one can use anharmonic oscillators with enough energy difference between pairwise levels such that the ground and first excited state can essentially be isolated, and exploited as the qubit basis states.
For superconducting qubits, this anharmonicity is introduced by exchanging the inductor of an LC oscillator with a Josephson junction (JJ), which can be modelled as a nonlinear inductor [15, 7]. The energy stored in the nonlinear Josephson junction is given by [4]

$$E = -E_J \cos\left(2\pi \frac{\Phi}{\Phi_0}\right), \tag{2.1}$$

where Φ is the node flux, related to the superconducting phase difference across the junction [5, 16], and

$$E_J = \frac{\Phi_0 I_c}{2\pi} \tag{2.2}$$

is the Josephson energy, with $\Phi_0 = h/2e$ the flux quanta, and I_c the junction's critical current. The Planck constant is denoted by h and the absolute electron charge by e. There is also a capacitance, C, in this anharmonic oscillator, which has an associated charging energy given by

$$E_C = \frac{e^2}{2C}. \tag{2.3}$$

[1] It is possible to use harmonic oscillators for quantum computing [11], which is a very exciting research field in itself but not the focus of my group. See for example [12, 13, 14].

For sufficiently large E_J/E_C ($>$ 50) the qubit's susceptibility to charge noise is reduced at the price of less anharmonicity; this type of superconducting qubit design is known as the transmon [17]. In Figure 2.1 we show the circuit diagram of the transmon, whose non-linear Josephson junction, depicted by a blue cross, is shunted by a large capacitance to decrease the charging energy, as given by Equation (2.3). This in turn increases the E_J/E_C ratio, decreasing the anharmonicity as well as the susceptibility to charge noise [17].

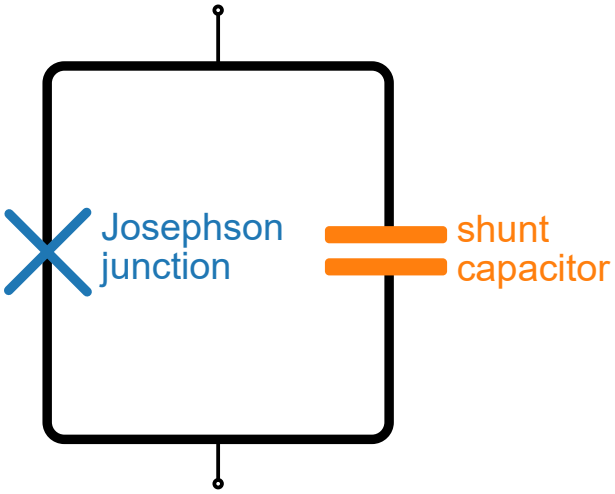

Figure 2.1: Circuit diagram of a transmon. The design is similar to an ordinary LC oscillator where the inductor has been replaced by the non-linear Josephson junction. Josephson junctions are depicted by a cross in circuit diagrams. The junction is shunted by a capacitor to increase the E_J/E_C ratio.

Assuming that the ground and first excited state of the transmon are completely isolated from the rest of the energy levels, their energy difference can be approximated as [5, 4]

$$\hbar\omega_q = \sqrt{8E_C E_J} - E_C, \tag{2.4}$$

where we define ω_q as the qubit's frequency. In reality, the first two energy levels are not completely isolated, and the transmon's dynamics are affected by higher energy levels [4, 18].

2.2 The frequency tunable transmon

Replacing the single Josephson junction in Figure 2.1 with a superconducting quantum interference device (SQUID) [15] allows for qubit frequency tuning by threading the SQUID loop with magnetic flux [4, 17, 5]. The Josephson energy of Equation

(2.2) can be replaced by

$$E_J \rightarrow E'_J \sqrt{\cos^2\left(\pi \frac{\Phi}{\Phi_0}\right) + d^2 \sin^2\left(\pi \frac{\Phi}{\Phi_0}\right)}, \tag{2.5}$$

where $E'_J = E_{J1} + E_{J2}$ is the sum of the individual junctions' Josephson energy, Φ is the flux threading the SQUID loop and $d = (E_{J1} - E_{J2})/E'_J$ is the SQUID's asymmetry parameter. The qubit frequency for a flux tunable transmon is in turn given by

$$\hbar\omega_q(\Phi) = \sqrt{8E_C E_J(\Phi)} - E_C. \tag{2.6}$$

Figure 2.2 shows the circuit diagram of a flux tunable transmon. The single Josephson junction in Figure 2.1 has been replaced by a SQUID, making the qubit frequency sensitive to flux threading the SQUID loop. A shunt capacitor is again incorporated to increase the E_J/E_C ratio. Flux can be applied to the SQUID by, for example, passing a current close by, such that the associated magnetic field threads the SQUID.

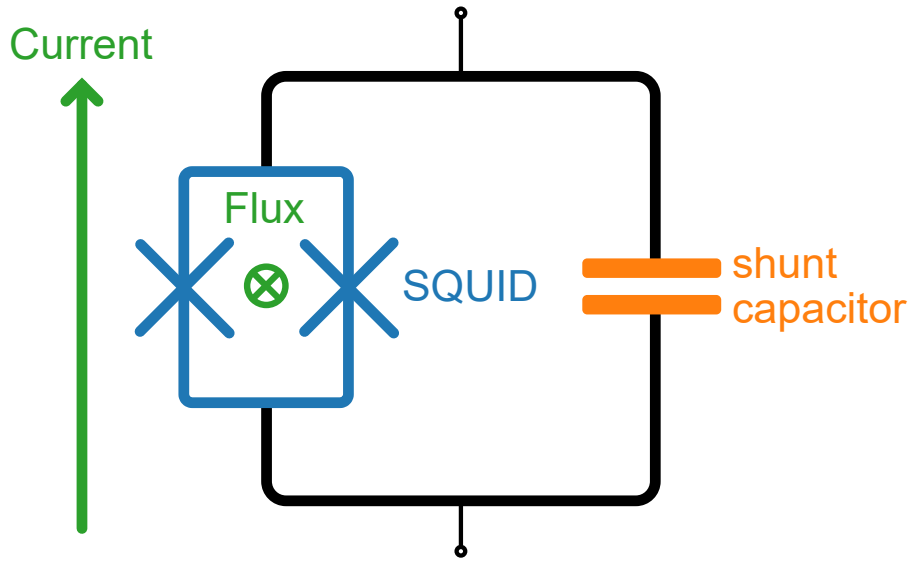

Figure 2.2: Circuit diagram of a frequency tunable transmon. Different colors depict different elements of the circuit. The single Josephson junction has been replaced by a SQUID. A current is sent close to the SQUID loop to induce magnetic flux through the loop.

2.3 Measuring a transmon

A qubit which has low E_J/E_C ratio can be directly addressed to measure which state it is in [19]. For the transmon, this is not possible due to the qubit's insuscep-

tibility to charge. Instead, the transmon is coupled to a harmonic oscillator, called a cavity, which generally is entangled with the qubit. The cavity is then probed to gain information about the qubit, minimising the readout's effect on the qubit and transferring the readout performance to cavity parameters instead of the qubit [5]. Truncating the qubit to a two-level-system, the Hamiltonian describing the qubit-cavity system is the well-known Jaynes-Cummings Hamiltonian [20, 1]

$$H = \omega_r a^\dagger a - \frac{\omega_q}{2}\sigma_z + g\left(a\sigma_+ + a^\dagger\sigma_-\right), \tag{2.7}$$

where the first term describes the cavity with frequency ω_r, the second term describes the qubit, and the third term denotes their interaction, with strength g. Note that we have written the Hamiltonian in terms of the cavity's annihilation and creation operators $(a, a^\dagger)$, and the qubit's lowering and raising operators (σ_-, σ_+). We have chosen $[\sigma_-, \sigma_+] = \sigma_z$, the Pauli Z matrix, as the qubit's quantisation axis.
The eigenvectors and eigenvalues of Equation (2.7) can be found analytically [1, 4] with the main result that the qubit and cavity are in general entangled. For information processing it is not useful to work in a regime where the qubit and cavity are strongly entangled, since tracing out the cavity would not give a pure qubit state. To mediate this, the qubit and cavity are far detuned with respect to their coupling rate, g, such that no direct energy exchange takes place between them [5, 4].
We can perturbatively diagonalise the Hamiltonian of Equation (2.7) by applying a Schrieffer-Wolff transformation $H \to e^S H e^{S^\dagger}$ with $S = \frac{g}{\Delta}\left(a\sigma_+ - a^\dagger\sigma_-\right)$, where $\Delta = \omega_q - \omega_r$. Omitting terms to the second order in $\frac{g}{\Delta}$ we find that

$$H \to \left(\omega_r - \chi\sigma_z\right) a^\dagger a - \frac{\omega_q'}{2}\sigma_z, \tag{2.8}$$

which is known as the dispersive regime of the Jaynes-Cummings Hamiltonian, with $\chi = \frac{g^2}{\Delta}$ the dispersive shift, and $\omega_q' = \omega_q + \chi$. Most importantly, we find that the effective cavity frequency has become dependent on the qubit state.
Now, we have a mean to infer the qubit state by probing the cavity coupled to the qubit. As given by Equation (2.8), the cavity frequency differs by 2χ depending on whether the qubit is in the ground or excited state. In circuit quantum electrodynamics (CQED), this system can for example be realised by capacitively coupling the qubit to a coplanar waveguide (CPW) resonator, which acts as the cavity [4]. In this case, probing the resonator means sending a signal at some frequency and measuring the reflected or transmitted signal. In the case of a $\lambda/4$ resonator, the resonator needs to be coupled to a transmission line, as schematically shown in Figure 2.3. The resonator is shown as an LC oscillator consisting of an inductor L_r and capacitor C_r, such that the bare resonance frequency is $\omega_r = \frac{1}{\sqrt{L_r C_r}}$. The resonator is coupled to the transmission line with rate γ and to the qubit by a capacitance C_c.

One can show that the forward scattering parameter, S_{21}, of the system depicted in Figure 2.3 with a $\lambda/4$ resonator, is given by [1]

$$S_{21}(\omega) = \frac{\frac{Q_e}{Q_e+Q_i} + 2iQ\frac{\omega-\omega_r'}{\omega_r'}}{1 + 2iQ\frac{\omega-\omega_r'}{\omega_r'}}, \tag{2.9}$$

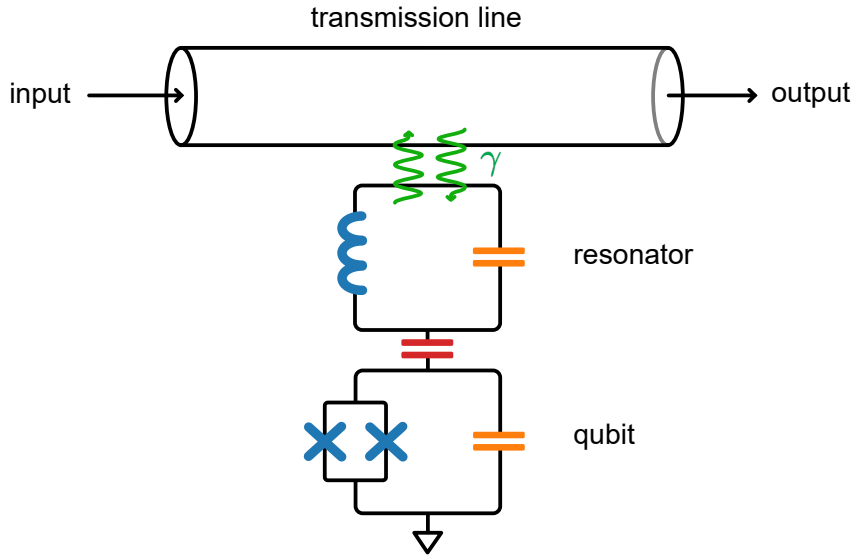

Figure 2.3: Circuit diagram of a qubit-resonator system coupled to a transmission line. A probe frequency is sent through the transmission line, the transmitted output will bear information about the qubit-resonator system, namely, it can be used to infer the qubit state. The qubit and resonator are capacitively coupled.

where we have defined $\omega_r' = \omega_r - \chi\sigma_z$ as the qubit state dependent resonator frequency and Q_e, Q_i as the resonator external and internal quality factors with $1/Q = 1/Q_i + 1/Q_e$. In Figure 2.4 we show how the transmitted signal looks depending on the qubit state, with different colors showcasing the transmission for different qubit states [21].
The calculation that we have presented for describing the qubit-cavity system is the simplest we can perform to gain qualitative understanding. A more thorough calculation would involve performing the Schrieffer-Wolff transformation before truncating the qubit to a two-level system [4]. When accounting for the transmons higher energy levels, one also finds a modification to the dispersive shift, given by [18]

$$\chi = \frac{g^2}{\Delta}\frac{\eta}{\Delta+\eta}, \tag{2.10}$$

where η is the qubit anharmonicity. An even further improvement would be to simply not perform any approximations and use the Cooper-pair box Hamiltonian [16], but that is not very convenient.

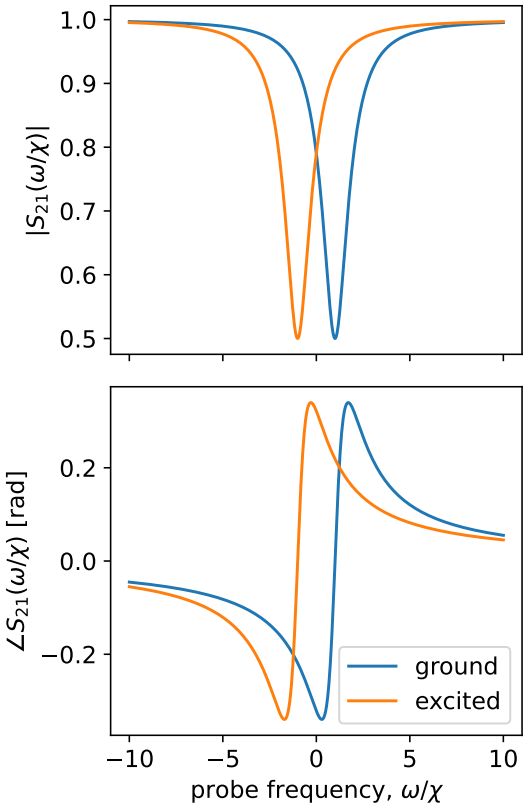

Figure 2.4: Amplitude and phase response of transmitted signal of a transmission line coupled to a qubit-resonator system. In this plot $Q_e = Q_i = 1$ and $\omega_r/\chi = 0$, with $\chi < 0$, i.e. $\omega_q < \omega_r$. The resonator exhibits qubit state-dependent resonance frequency.

2.4 Flux pulse distortions

As mentioned in Section 2.2, in the case of a tunable transmon, we need to send flux through the SQUID in order to tune the qubit's frequency. The flux is usually applied as a voltage pulse, whose waveform is generated at room temperature, but traverses through multiple electrical components and temperature stages before reaching the qubit. These elements all distort the pulse [22, 23]; moreover, on-chip impedance mismatch [24] or flux buildup [25, 26, 27] also contribute to the distortion of the pulse, further complicating the model we try to impose on the resulting distortions. Abstractly, a distortion is modelled as a transfer function, $h(t)$, acting on our input, $x(t)$, resulting in an output

$$y(t) = h(t) * x(t), \tag{2.11}$$

where $*$ denotes convolution. In frequency or Laplace space, Equation (2.11) takes the simple multiplication form $Y(s) = H(s)X(s)$, where capital letters denote the Laplace transforms of y, h and x respectively, with s as the complex variable. This formulation makes it convenient to characterise step responses when the transfer function $H(s)$ is known, since the Heaviside-theta function $x(t) = \theta(t)$ corresponds in Laplace space to $X(s) = 1/s$, and the output is simply given by $Y(s) = H(s)/s$. Correcting for distortions essentially boils down to characterising $h(t)$ and designing a filter which transfers $x(t) \to h_{\text{inv}}(t) * x(t)$ such that

$$y(t) = h(t) * [h_{\text{inv}}(t) * x(t)] \approx x(t), \tag{2.12}$$

as accurately as possible. There are two types of digital filters we can use to apply $h_{\text{inv}}(t)$ to our input. They are known as finite impulse response (FIR) filters, and infinite impulse response (IIR) filters [23]. Each type has its own advantages and disadvantages, discussed in the next subsections.

2.4.1 Finite impulse response filters

Finite impulse response (FIR) filters perform a convolution on the input by summing the products of N previous inputs weighted by the filters coefficients. In digital domain, this is expressed as [23]

$$y[n] = \sum_{i=0}^{N} h[i]x[n-i], \tag{2.13}$$

where $y[n]$ is the output, N is the filter order, $h[n]$ are the filter coefficients and $x[n]$ is the input signal. The FIR filter coefficients are synonymous with the system's impulse response [28].

The design of an FIR filter was done without directly measuring the transfer function, $h[n]$. Instead, the output, $y[n]$, was measured and a least squares algorithm run which searched for the vector $h_{\text{inv}}[n]$, which when applied to $y[n]$ resulted in $x[n]$. In this work the length of $h_{\text{inv}}[n]$ was kept the same as the length of $y[n]$ since we were not limited by hardware when applying the FIR filter.

The main advantage of FIR filters is that they are stable, while their disadvantage is that they are susceptible to imperfect measurements of the transfer function [29]. Indeed, FIR filters can only correct for reproducible distortions and not noise.

2.4.2 Infinite impulse response filters

The other type of digital filter is the infinite impulse response (IIR) filter. The fundamental difference between IIR and FIR filters is that IIR filters always require feedback [23]. IIR filters are defined by a set of coefficients $a[n]$ and $b[n]$ describing the discrete time-domain difference equation

$$y[n] = \sum_{i=0}^{N} b[i]x[n-i] + \sum_{i=1}^{M} a[i]y[n-i], \tag{2.14}$$

where M is the IIR filter's order. In continuous Laplace-space, Equation (2.14) is given by

$$Y(s) = \frac{\sum_{i=0}^{N} b_i s^i}{\sum_{i=0}^{M} a_i s^i} X(s), \tag{2.15}$$

which relates the transfer function, $H(s)$, to the coefficients a and b. Equation (2.15) lives in continuous space, but our pulses are discrete, since they are generated by an arbitrary waveform generator (AWG). As we discuss later, and show in Appendix A, the analysis is the same as there is a simple conversion between continuous and discrete space. Continuous and discrete coefficients, a and b, are not the same numbers, however.

To relate Equation (2.14) to something tangible, let us model the qubit as an RLC circuit, i.e. a second order system [28]. A signal sent to the qubit will therefore be convoluted by a two-pole transfer function, which can in general be written in the Laplace-domain as [23]

$$H(s) = \frac{A_0}{s + p_0} + \frac{A_1}{s + p_1}. \tag{2.16}$$

We can calculate the time-domain step response by taking the inverse Laplace transform of $\frac{H(s)}{s}$ [28] to find

$$s(t) = 1 + a_0 e^{-t/\tau_0} + a_1 e^{-t/\tau_1}, \tag{2.17}$$

where $a_i = -A_i/p_i$ and $\tau_i = p_i^{-1}$, with $i \in \{0, 1\}$. From Equation (2.17), we see that there is a simple way of characterising IIR filters by measuring the system's step response. To correct for the distortion we simply apply the inverse transfer function $1/H(s)$ to our input.

There is one more caveat we need to take care of before predistorting with IIR filters. This is the transformation from continuous to digital domain. Indeed, the step response characterises the continuous transfer function but the signal we send is digital, so we need to convert our continuous transfer function to the digital domain. There are different ways of achieving this, with the bilinear transform a very convenient method since we simply replace s as a function of the digital variable, z. The bilinear transform is given by

$$s \to \frac{2}{t_s}\left(\frac{1 - z^{-1}}{1 + z^{-1}}\right), \tag{2.18}$$

where t_s is the sampling time. Importantly, this transformation maps stable filters in the continuous domain to stable filters in the digital domain [23]. Once we have digitised our filter, the job is done, and we can apply the filter to our waveform.

2.5 Two-level-system defects

The qubit is necessarily coupled to its control environment. There is also another environment to which the qubit couples to against our will. This is the *evil* environment whose impact engineers try to minimise with changes in fabrication, shielding and design.
One of the mechanisms found to be a dominating limit to transmon coherence are two-level-system (TLS) defects [30, 9, 31]. TLSs are described using the standard tunnelling model, which can be visualised as a particle in double-well parabolic potential [9]. This is shown in Figure 2.5 where the particle is assumed to be able to hop with rate Δ_0 between two energy levels, which are seperated by energy ε. The energy difference between the particle's eigenstates can easily be found by diagonalising a 2x2 Hamiltonian and is $E = \sqrt{\varepsilon^2 + \Delta_0^2}$.

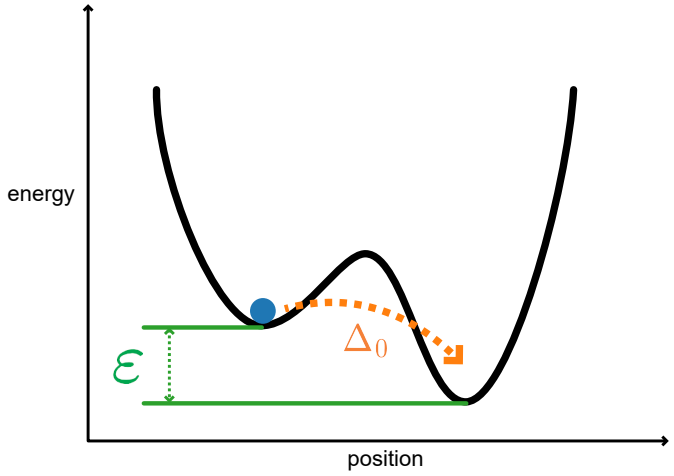

Figure 2.5: Particle in a double-well potential. The asymmetry between the two wells is shown with ε, and Δ_0 describes the tunnelling rate between the two wells. The particle's transition energy is given by $E = \sqrt{\varepsilon^2 + \Delta_0^2}$.

The standard tunnelling model has great utility, being able to predict both low-frequency and high-frequency noise by creating TLS ensembles and looking at their interaction [32]. However, it does not give us any intuition for what a TLS is, microscopically. Knowing what TLSs are might help us remove them or decrease their coupling to the qubit.
In this thesis, we discuss TLSs as if they are spurious qubits, interacting with our fabricated qubit against our will. The TLS has some energy seperation between its two eigenstates, just like our qubit, and the TLS and qubit can interact. The two systems also decay with their own rates Γ_Q and Γ_TLS, respectively. For an as exact model as possible we would construct the 3x3 Hamiltonian in the basis $\{|0\rangle, |\mathrm{qubit}\rangle, |\mathrm{TLS}\rangle\}$, for example, where $|0\rangle$ denotes the environment in which the qubit and TLS can decay to.
Solving 3x3 Hamiltonians is difficult. We can decrease the computational subspace to 2x2 by using a non-Hermitian Hamiltonian [33, 34] to model the decay of proba-

bility to the environment. We define the system Hamiltonian as

$$H = \begin{pmatrix} \omega_{\mathrm{Q}} - i\frac{\Gamma_{\mathrm{Q}}}{2} & g \\ g & \omega_{\mathrm{TLS}} - i\frac{\Gamma_{\mathrm{TLS}}}{2} \end{pmatrix}, \tag{2.19}$$

describing the decay of the qubit and TLS, and their interaction. The eigenvalues of non-Hermitian Hamiltonians will in general be complex. We can write the time evolution of an arbitrary state, $|\psi\rangle$, as[2]

$$|\psi(t)\rangle = e^{-iHt}|\psi\rangle = \sum_n e^{-i\lambda_n t} c_n |\phi_n\rangle = \sum_n e^{-i\,\mathrm{Re}(\lambda_n)t} e^{\mathrm{Im}(\lambda_n)t} c_n |\phi_n\rangle, \tag{2.20}$$

where it becomes clear that the imaginary part of the eigenvalues correspond to the decay or growth of the state. Also note that decay or growth rates are defined with respect to the decay or growth of probabilities, which is why there is a factor half in the decay rates in Equation (2.19). The calculation shown in Equation (2.20) is also just for qualitative explanation, it actually is not guaranteed that the eigenstates of a non-Hermitian Hamiltonian are complete, so we might not be able to expand the initial state, $|\psi\rangle$, in the eigenbasis of the Hamiltonian.
There are three defining parameters in Equation (2.19); the qubit decay rate Γ_{Q}, the TLS decay rate Γ_{TLS} and their interaction strength g. We can split the Hamiltonian into $H_0 + g\sigma_x$, where σ_x is the Pauli X matrix and, if $g << \frac{\Gamma_{\mathrm{TLS}}}{2} - \frac{\Gamma_{\mathrm{Q}}}{2}$, we can use perturbation theory to find the eigenenergies of the system. Up to second order (first order correction is zero), we find an effective qubit decay rate given by

$$\Gamma_{\mathrm{eff}} = \frac{2\frac{g^2}{\Gamma}}{1 + \left(\frac{\Delta}{\Gamma}\right)^2} + \Gamma_{\mathrm{Q}}, \tag{2.21}$$

where $\Gamma = \frac{\Gamma_{\mathrm{TLS}}}{2} - \frac{\Gamma_{\mathrm{Q}}}{2}$ and $\Delta = \omega_{\mathrm{Q}} - \omega_{\mathrm{TLS}}$ is the qubit-TLS detuning. The step-by-step derivation of Equation (2.21) is shown in Appendix B.
Equation (2.21) states that the effective qubit decay rate increases as g^2 and decreases if the TLS decay rate is increased. At first, this seems counterintuitive since it seems logical that if the TLS decays faster, the qubit should acquire a faster effective decay rate. This is not the case and can be explained by looking at the system's density matrix as shown in Figure 2.6. The scaling of the effective qubit decay rate is described by first noting that coherence needs to be built up before direct energy can be exchanged between the qubit and TLS. This, we refer to as coherent swapping. Since the qubit and TLS interact with rate g, the coherent information can be built up with rate g, and then swapped to the TLS, also with rate g, leading to a net $|\mathrm{qubit}\rangle\langle\mathrm{qubit}| \rightarrow |\mathrm{TLS}\rangle\langle\mathrm{TLS}|$ swapping rate of g^2.
Now, the TLS and qubit have their own decay rate and therefore a dephasing rate as well [5]. This dephasing rate causes the coherent information to be lost into the environment, if the dephasing rate is much faster than g, the coherence will not be built up between the two states and they can not swap their excitation. The TLS decay rate does not increase the effective qubit decay rate due to the dephasing it carries with it.

[2] Assuming a time-independent Hamiltonian

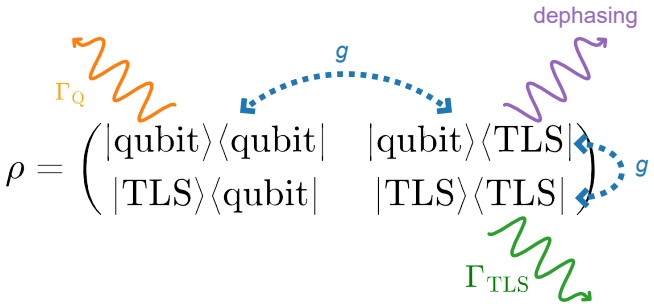

Figure 2.6: A schematic depiction of how coherent information needs to be built up before the qubit can decay through the TLS. The rate g is a probabilistic rate such that the effective rate $|\text{qubit}\rangle\langle\text{qubit}| \rightarrow |\text{TLS}\rangle\langle\text{TLS}|$ is g^2. If the dephasing, shown in purple, is greater than the rate g, the excitation will not be able to swap from qubit to TLS.

In Figure 2.7 we showcase the result using the energy levels of the system and how the qubit effectively decays through the TLS. The fact that the qubit has to travel through the TLS implies that we can gain some information of the TLS by measuring the qubit's effective decay rate.

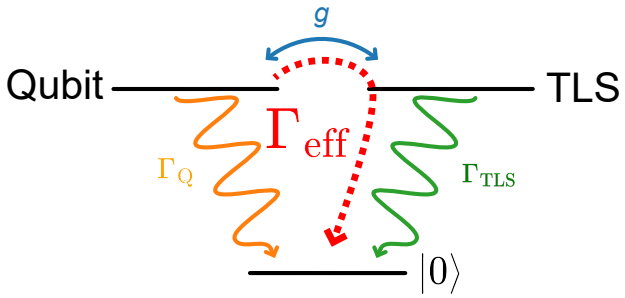

Figure 2.7: The qubit acquires an effective decay rate, Γ_{eff}, through the TLS when a swapping interaction g turns on between the qubit and TLS. This visualisation is only correct if the TLS decay rate is much faster than the swapping rate and the qubit decay rate.

The results of this section are only valid in the regime where $g << \Gamma_{TLS}/2 - \Gamma_Q/2$, and since $g > 0$, we necessarily have that $\Gamma_{TLS} > \Gamma_Q$. Clearly, the qubit decay rate must be the smallest parameter, otherwise the qubit would just decay on its own and never interact with the TLS. There is, therefore, a hierarchy of parameters which leads to a measurement technique susceptible to TLSs with parameters in the range $\Gamma_Q < g < \Gamma_{TLS}$.

2.6 Quasiparticles

The superconducting fluid in our device is made up of Cooper pairs, which are electron pairs forming a boson-like fluid [15].[3] This pairing was shown to be possible if the interaction between electrons is sufficiently weak. Cooper essentially showed that the Fermi sea of electrons is not stable, since a perturbation moving two electrons above the Fermi energy will allow the two electrons to bind and form the energetically favorable Cooper pair, reducing the system energy. The Cooper pairs are mediated by virtual phonons, which together with the fact that the electron-electron interaction must be weak, indicates that *bad* metals are *good* superconductors [35]. Importantly, Cooper pairs are composed of electrons with opposite momentum and spin.

At absolute zero, all electrons close to the Fermi level form the favoured Cooper pair, opening up a gap, Δ_{sc}, in the electron density of states around the Fermi energy. At finite temperature, the superconducting condensate is expected to contain excitations due to the thermal energy [36, 37]. These excitations are called Bogoliubov quasiparticles (QPs) and describe broken Cooper pairs. These QPs are a superposition of an electron and a hole [15], which stems from the fact that, even at zero temperature, the probability of electrons being paired in Cooper pairs is blurry around the Fermi level [35]. This probability of being both electron and hole should simply be pictured as the ensemble average; for individual ensemble members, each QP is either an electron or hole.

To get an intuitive picture of what happens when a Cooper pair breaks, we draw the excitation energy of the system in Figure 2.8. Note that the excitation energy is positive in both directions, with the pink-redish color showcasing the states filled by electrons. Electron particles are drawn as black spheres with corresponding white spherical holes. Since the Cooper pair is made up of two electrons, an excitation from the superconducting ground state should necessarily include both positive and negative electron momentum. Furthermore, to conserve electrons, quasiparticle excitations must come in pairs symmetrically located around the Fermi level [35]. Generally, the QPs will be a superposition of an electron and a hole, but if they are sufficiently far away from the Fermi level, we can point to the one which is an electron and the one which is a hole with good accuracy. This superposition characteristic is shown in Figure 2.8 as differently sized spheres of the two QPs, the one which is an electron most of the time has a larger black sphere, and the one which is a hole most of the time has a larger white sphere.

The sublety of a QP being a superposition of an electron and a hole, does not play a part in the tunnelling dynamics in Josephson junctions. This is because the probability of *either* of two states symmetrically located around the Fermi wave vector, k_F, have unit probability to be vacant. In the context of counting tunnelling currents, it is therefore fine to assume all states below k_F to be filled and states above k_F to be empty [35]. With respect to Figure 2.8 we can say that, if we know one of the QPs turned out to be an electron, we know that the other one is a hole. The quasiparticles contribute to the qubit relaxation rate and dephasing, as well

[3] The Cooper pairs are not exactly bosons since the Pauli principle applies to them, but they are close enough to bosons that boson electrodynamics can sometimes be applied.

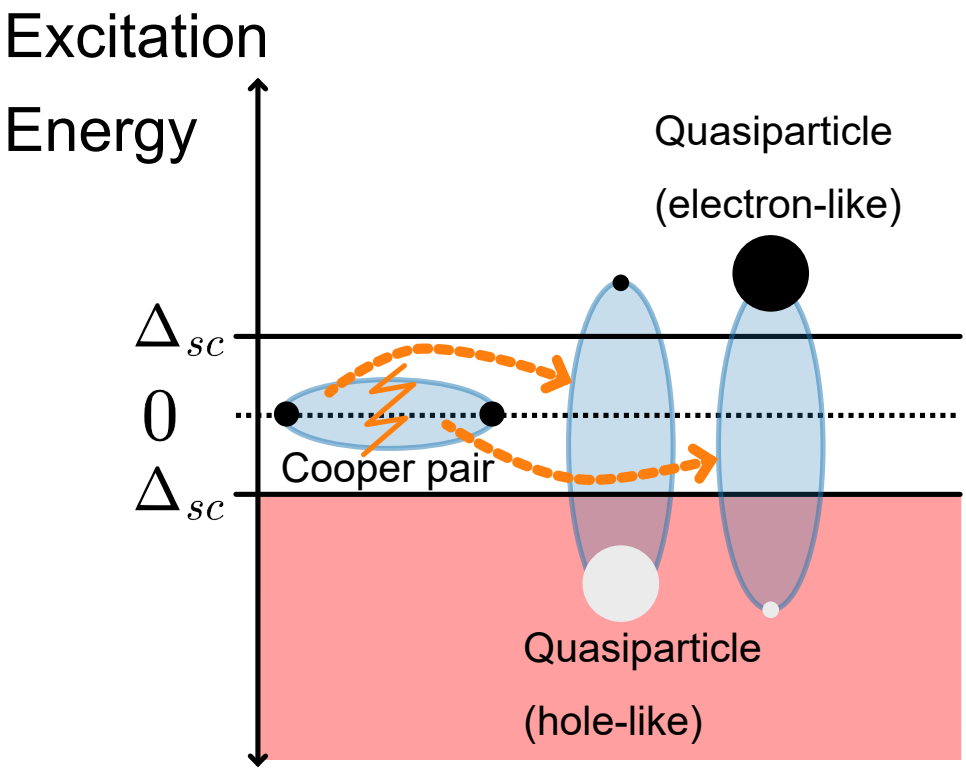

Figure 2.8: A schematic representation of how a Cooper pair is broken into two quasiparticles. The y axis depicts the excitation energy, positive in both directions, to include electron and hole excitations. Generally, the two quasiparticles are both a superposition of an electron and a hole. The different probabilities are represented as different sizes of the electron and hole spheres. To conserve electron number, the Cooper pair is broken into quasiparticles symmetrically distributed around the Fermi level, such that if one of the quasiparticles is hole-like, the other quasiparticle will be electron-like.

as the residual excited state population of the qubit [38, 39, 40, 41, 42], since the electron excitation we created in Figure 2.8 can tunnel over the junction. The QPs are fermions, so their distribution is described by the Fermi-Dirac distribution, and because of the gap, Δ_{sc}, the number of QPs is expected to be exponentially small ($\sim e^{-\Delta_{sc}/k_B T}$), and the losses associated with them should therefore be small [43].
In Figure 2.9 we show three different processes, labelled (a), (b) and (c), which change the charge in both of the superconducting leads of the superconductor-insulator-superconductor (SIS) junction. Compared to Figure 2.8, Figure 2.9 only shows the electron-like excitation side, but we still allow ourselves to draw the hole-part of the QPs for clarification.[4] We have also added the QP density of states [35]. There are essentially two types of proccesses to consider, the electron from a broken Cooper pair can tunnel over the junction, or a Cooper pair may be broken, injecting a QP in both superconducting leads [44, 42].
The process labelled (a) in Figure 2.9 depicts the event of the qubit relaxing, emitting a photon of frequency f_{Q}, exciting an electron, and the electron tunnelling over the insulator. This process is detrimental to quantum information processing since it limits the qubits inherent relaxation time [39]. The electron can also tunnel over the junction without absorbing a photon from the qubit, as shown in the process labelled (b), in Figure 2.9. While this process does not cause qubit relaxation, it does contribute to qubit dephasing [10]. The final process is labelled (c) in Figure 2.9 and depicts the breaking of a Cooper pair by a stray photon of frequency greater than $2\Delta_{sc}$. The QPs are then deposited in each of the superconducting leads, changing their parity [42, 44].
Either of the superconducting leads in Figure 2.9 corresponds to the superconducting qubit pad, while the other corresponds to the ground plane. When any of the processes depicted in Figure 2.9 take place, the parity of the qubit lead changes by $\pm e$. For a transmon with large E_J/E_C ratio, this parity change is not felt due to the non-susceptibility to charge, until high excitations are reached [17]. A qubit with lower E_J/E_C ratio will, however, be sensitive to these changes in charge. The energy diagram of a charge sensitive qubit is schematically shown in Figure 2.10 where we see the presence of two transitions with an energy difference. Instead of shifting the energy levels by $\pm e$, we can imagine there are two ground and excited levels corresponding to even and odd parity. When the parity of the qubit pad changes from even to odd, or vice versa, the qubit transition frequency changes as well. The qubit can also move its position along the charge offset axis due to background charge fluctuations.

[4] We can imagine that we take the top and bottom of Figure 2.8 and fold it onto itself.

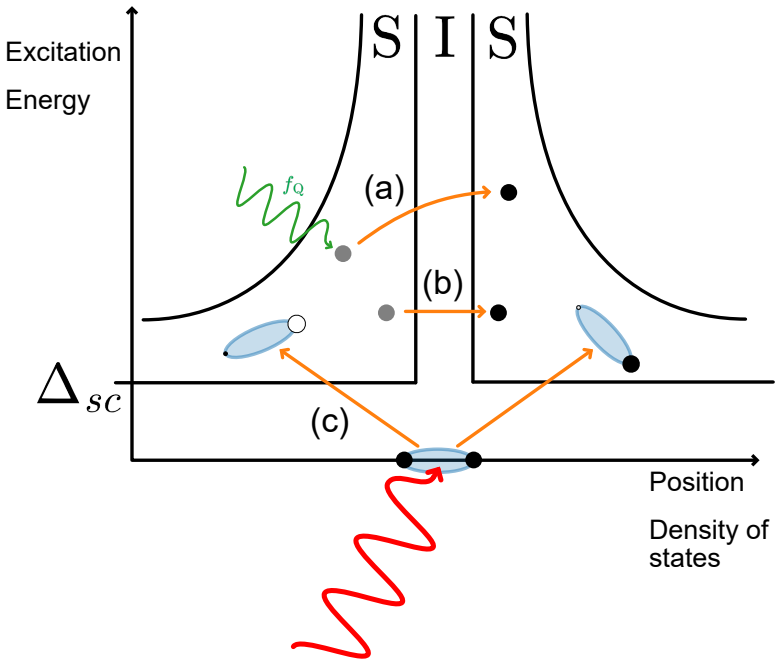

Figure 2.9: Possible QP tunnelling processes over a superconductor-insulator-superconductor (SIS) barrier. The QP can (a) absorb a photon from the qubit, with frequency f_Q, and tunnel over the junction, inducing qubit relaxation. The QP can also (b) tunnel over the junction without inducing qubit relaxation but causing qubit dephasing. (c) A high energy photon with frequency greater than $2\Delta_{sc}$ can impinge on a Cooper pair and break it into two QPs which are deposited in each superconducting lead.

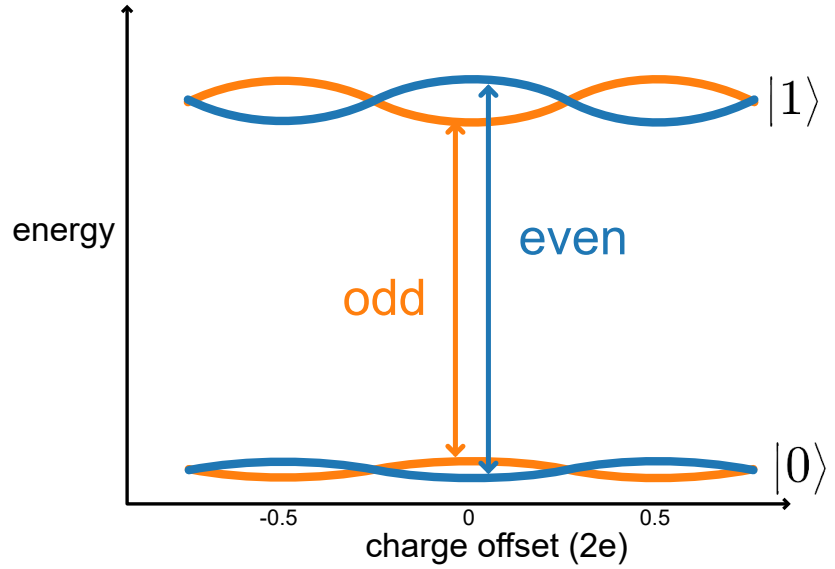

Figure 2.10: A transmon's sensitivity to charge offset. The difference between even and odd parity transitions is exponentially suppressed with increasing E_J/E_C ratio. The energy levels have periodicity $2e$. When a QP tunnels over the junction, the offset charge changes by $\pm e$, shifting the energy level curve by $\pm e$, which is visualised as switching between even and odd parities.

2.7 Purcell decay

An atom in a cavity experiences either enhanced or suppressed emission rates due to the reflected atomic radiation exciting the atom out of phase, or in phase [45].[5] This effect is known as the Purcell effect, named after Purcell, who first studied it in the context of two-level-systems coupled to circuits [46]. Under a single-mode approximation of the cavity, it can be shown that the rate of decay of the atom due to the Purcell effect is given by [47, 48]

$$\Gamma_p = \kappa \frac{g^2}{\Delta^2}, \tag{2.22}$$

where κ is the cavity decay rate, g is the coupling between atom and cavity, and Δ is the detuning between atom and cavity. In the context of superconducting circuits, Equation (2.22) is often visualised as the tail of the qubit wavefunction existing as a resonator photon and therefore being able to decay through the resonator [5]. Equation (2.22) is an approximation, indeed, and it has been shown that incorporating all of the cavity's modes into the model is crucial to obtaining experimentally verifiable results [49]. Incorporating all of the cavity's modes also explains why operating in the negative qubit-resonator detuning regime ($\Delta = \omega_q - \omega_r < 0$) is preferable, as the cavity decay rate is larger for higher harmonics and the coupling to higher order modes is increased, compared to the fundamental mode.

[5] This is more commonly attributed to a change in the local density of states of the cavity. Fermi's golden rule then reminds us that the decay rate is proportional to the density of states of the final state.

For the superconducting circuits measured in this project, the coupling, g, between qubit and resonator is dependent on the qubit and resonator frequencies, since it originates from the capacitive coupling with a frequency dependent impedance [50]. To account for this, Equation (2.22), can be modified as

$$\Gamma_p = \kappa \frac{C_g^2}{4C_q C_r} \frac{\omega_q \omega_r}{(\omega_q - \omega_r)^2}, \tag{2.23}$$

where C_g is the coupling capacitance and C_q, C_r are the qubit and resonator capacitances, respectively.

3

Methods

In this chapter we present some practical aspects of the project. First, we show the experimental setup and mention which equipment was used. We describe the designs of the measured devices. We show the pulse sequences for all measurements, including the flux pulse characterisation experiments, TLS spectroscopy, how the parity switches were monitored and how the Purcell decay was characterised.

3.1 Experimental setup

All measurements were conducted in Lumi, an LD400 dilution refrigerator from Bluefors with a guaranteed base temperature of 10 mK [51]. The fridge connections and electrical components used are shown in Figure 3.1. Input signals were generated by an M3202A PXIe AWG from Keysight, with a 1 GS/s sampling rate, 12 bit resolution and 400 MHz bandwidth. The signals were upconverted to the qubit-resonator GHz regime by mixing the AWG signals with a SGS100A RF source local oscillator (LO) from Rohde and Schwarz.

Upon entering the fridge, the signals were attenuated and filtered in the different stages of the fridge, as shown in Figure 3.1. The total attenuation needed to suppress thermal noise was distributed among different stages to minimise active load on lower stages, such that the load was less than the available cooling power [52]. Low-pass (LP) filters were implemented to remove high frequency noise and higher harmonics of the mixer output. Eccosorb microwave absorbers reduce the effect of infrared radiation by attenuating high-frequency signals.

After the signal transmits through the chip, it was LP and high-pass (HP) filtered with isolators between the filters as shown in Figure 3.1. Isolators prevent signal backflow to the device. The signal was then amplified with a low-noise amplifier (LNA) before going through 0 dB attenuators. The LNA used in this project was the LNF-LNC4-8C s/n 184A from Low Noise Factory. Before the signal was digitised, it was further amplified at room temperature and down-converted to the digitisers bandwidth. The digitiser used was an M3102A PXIe digitiser from Keysight with 500 MS/s sampling rate, 14 bit resolution and 200 MHz bandwidth. Triggering was done internally using the Keysight software, Labber, as well as sequence generation [53].

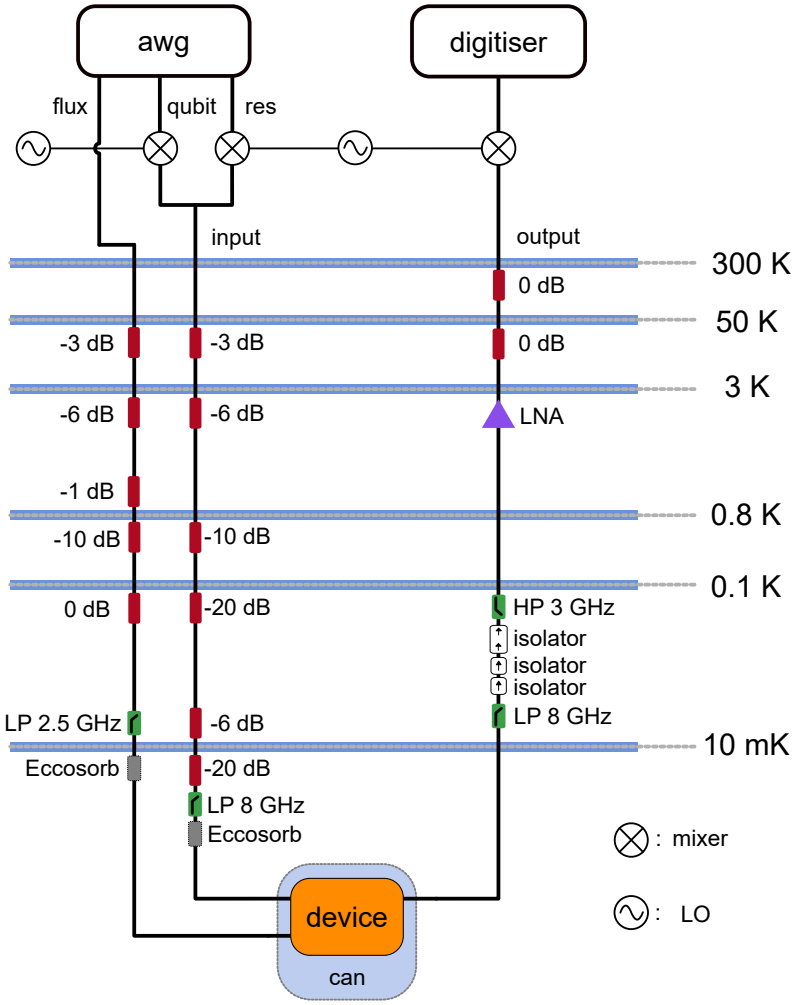

Figure 3.1: Schematic of fridge connections. The resonator (res) and qubit signals were upconverted by their respective LOs before being sent to the sample. The output was downconverted with the resonator's LO to the digitiser's bandwidth. The device was mounted in a sampleholder and placed in a copper can inside a mu-metal shield.

3.2 Devices

Results presented in this thesis were measured on two different chips. The chip used for flux pulse characterisation and TLS spectroscopy was previously fabricated for studying the fabrication reproducibility of thin and thick oxide junctions [54]. Note that none of the devices reported on in this thesis had a designated XY drive line for the qubit. To rotate the qubit around the X or Y axis on the Bloch sphere, a pulse was sent through the feedline and resonator. From the feedline, through the resonator and to the qubit is significant attenuation, and so XY rotations without drivelines require pulses with more photons than pulses through a dedicated driveline. This is why pulses in this thesis are considerably longer than pulses applied to qubits via a driveline.
For QP tunnelling measurements and Purcell decay characterisation we measured another, newly fabricated chip. The qubits were specifically designed for their respective experiments, as we will now describe. Along with discussing the design, we present relevant parameters extracted from calibration measurements in the coming subsections.

3.2.1 Frequency tunable transmon

The tunable qubit is sensitive to applied flux, so the resonator will also shift with applied flux.[1] We need to take care of this when we perform the initial qubit-flux calibration since we calibrate the qubit for DC flux offsets to avoid distortion effects. When the readout pulse is applied, the qubit is still being flux biased, and therefore the dressed resonator frequency will be affected. This means that we first need the resonator frequency as a function of flux before we can find the qubit frequency as a function of flux.
Figure 3.2 shows the tunable qubit frequency as a function of applied flux, in the top panel we see peaks corresponding to the qubit transition frequencies. The qubit frequency was fit to Equation (2.6), as shown in the middle panel of Figure 3.2, with the error shown in the bottom panel as the difference between the fit and measured points.
The optimal fit parameters are shown in Table 3.1, where $d\Phi/dV$ denotes the flux to voltage conversion and V_0 is the voltage needed to bias the qubit to the first order flux insensitive point. We fixed E_C to 200 MHz, as the designed value, since it is expected to be close to the design value. This reduces the number of free parameters, simplifying the fitting process.

[1] Remember the dispersive shift $\chi = g^2/\Delta$ is dependent on the qubit-resonator detuning. Changing the qubit frequency changes the detuning, and therefore the dressed resonator frequency although the resonator is not sensitive to applied flux at all.

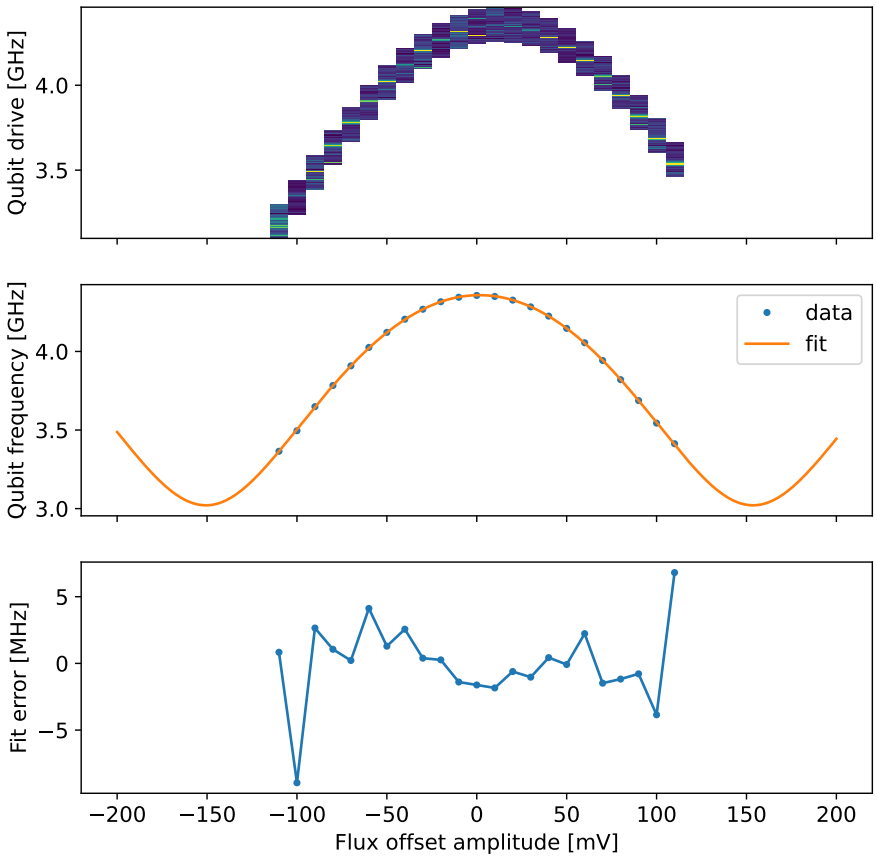

Figure 3.2: Qubit spectroscopy of the tunable transmon with applied flux. Top panel shows the qubit spectroscopy measurement result. The extracted qubit frequencies as a function of flux are shown in the middle panel along with the best fit. The bottom panel shows the error between measured qubit frequencies and frequencies predicted via the fit.

Table 3.1: Parameters found from fitting qubit frequency as a function of DC flux offset with E_C forced to 200 MHz. Here, $f_{01}^{\max}$ is the qubit frequency at the flux-insensitive point, E_J/E_C is the ratio at the flux insensitive point, d is the asymmetry parameter, $d\Phi/dV$ is the conversion constant from voltage to flux, and V_0 is the voltage bias needed to tune the qubit to the flux insensitive point.

$f_{01}^{\max}$	E_C	E_J/E_C	d	$d\Phi/dV$	V_0
4.357 GHz	200 MHz	64.9	0.499	3.287 Φ_0/V	1.519 mV

3.2.2 QP transmon

The transmon designed for measuring quasiparticle tunnelling events had intentionally lower E_J/E_C ratio. This made the transmon sensitive to changes in the charge offset, a key ingredient for measuring quasiparticle tunnelling [37, 36, 55]. The qubit was calibrated using standard procedures, with average qubit frequency measured as $f = 3.7922$ GHz. With the designed $E_C = 307$ MHz, this corresponds to $E_J/E_C \sim 22$.[2] Solving for the charge dispersion, using the Mathieu functions which exactly describe the eigenenergies [17], results in an estimated $2\Delta f \sim 2.39$ MHz detuning between the even and odd qubit parity states.

3.2.3 Purcell transmon

The transmon fabricated for empirically characterising the Purcell decay was designed such that the qubit could be tuned through the resonator while also having as much detuning range as possible. This was achieved by designing the transmon to have a high maximum frequency, higher than the resonator, and making the SQUID symmetric. In theory, this would allow the qubit frequency to be varied from 7.5 GHz all the way down to zero. In practice, our fabricated device was able to produce qubit-resonator detunings shown in Figure 3.3. All measurements of the Purcell transmon were done with DC flux offsets to avoid predistortion effects and to encompass all coupling strengths. If a flux pulse were used instead, we would set a lower bound for the coupling strengths which could interact with the qubit, approximately as the inverse of the pulse duration.

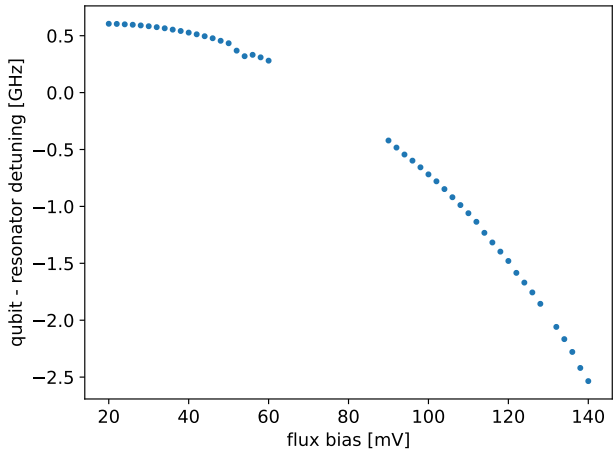

Figure 3.3: Measured available qubit-resonator detuning of the transmon specifically designed for empirically characterising the Purcell effect. The available detuning range was limited by the resonators dispersive shift, that at large detunings becomes too small. At small detunings the qubit and resonator directly exchange energy and the system exits the dispersive regime.

[2]This estimation is calculated using the approximation $f = \sqrt{8E_JE_C} - E_C$.

3.3 Flux pulse characterisation

As shown in Figure 3.1 there are many electrical components in the fridge. In this section we describe two methods that can be used for characterising how these components distort a square flux pulse used for tuning the qubit frequency. These two methods are referred to as pulse wrapping and Cryoscope.

3.3.1 Pulse wrapping

Applying flux to the qubits SQUID changes the qubit frequency. In Subsection 3.2.1, we mentioned that a spectroscopy measurement can be performed to find the qubit frequency. This type of measurement can also be used to measure the flux pulse's distortion if we are able to calibrate the qubit-flux dependence in the absence of any distortions. To achieve this, we calibrate the qubit-flux dependence using DC flux offsets and perform qubit spectroscopy *inside* a flux pulse to see how the qubit frequency varies due to distortion effects compared to the DC offset reference. We refer to this method of measuring flux pulse distortions as pulse wrapping, since a spectroscopy pulse is wrapped in a flux pulse.
Figure 3.4 shows the pulse sequence for the pulse wrapping method [56]. A spectroscopical X pulse with varying frequency is sent to the qubit, after which we readout its state. This simply describes a two-tone spectroscopy measurement. To measure flux pulse distortions, the X pulse is wrapped in a flux pulse, Φ, of varying duration Δt. As Δt is swept we measure the qubit frequency for different positions inside the flux pulse. From our DC flux offset calibration, we have a reference for which qubit frequency we *should* measure for the applied flux pulse. Comparing to the calibration, we extract the flux pulse step response and infer the distortions.

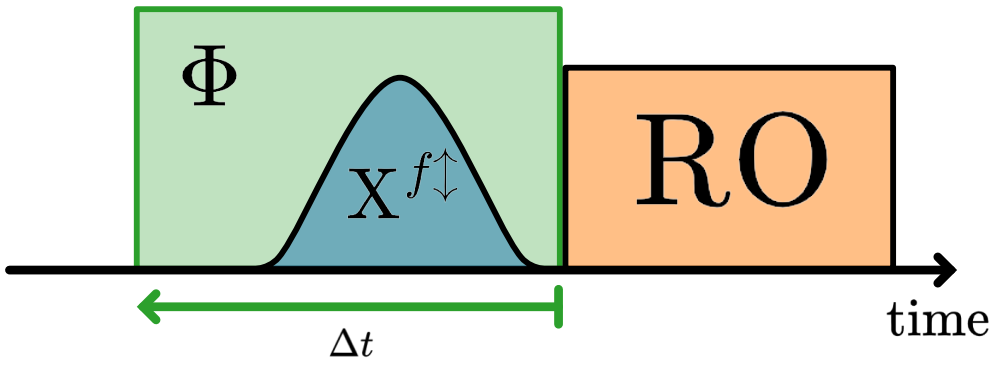

Figure 3.4: Sequence of the pulse wrapping method. An X pulse with varying frequency, f, is wrapped in a flux pulse, Φ, after which the qubit state is read out (RO). This is effectively a two-tone spectroscopy measurement inside a flux pulse. Sweeping Δt allows us to measure the qubit frequency step response.

The limit of the pulse wrapping method is the duration of the qubit tone we send, X. The extracted qubit frequency will be some kind of weighted average of the qubit frequency during the whole X pulse.

3.3.2 Cryoscope

Another method of measuring flux pulse distortions is to analyse the accumulated qubit phase during, or after, a flux pulse [24, 57]. Imagine we begin with a qubit in the ground state and then put it on the equator with a $\pi/2$ pulse. In the frame rotating at the drive frequency, the qubit will not rotate around the Z axis since we applied the $\pi/2$ pulse on resonance. However, if we then apply a flux pulse after the $\pi/2$ pulse, the qubit will begin to rotate with a frequency given by the detuning that the flux pulse applies to the qubit frequency. If we then turn the flux pulse off and apply a qubit tomography pulse, we can measure the qubit position in the $\langle X\rangle$-$\langle Y\rangle$ plane on the Bloch sphere, after the flux pulse. We can use the qubit's position in the $\langle X\rangle$-$\langle Y\rangle$ plane to infer how much phase the qubit accumulated during the flux pulse and translate that into how much detuning the flux pulse applied.
This is the idea of the Cryoscope technique [24], which is implemented with the pulse sequence in Figure 3.5. Initially, the qubit is placed on the equator with a $\pi/2$ pulse and then let rotate around the Z axis with a flux pulse Φ with variable duration Δt. The seperation between the initial $\pi/2$ pulse and the tomography pulse after the flux pulse is kept fixed at T_{sep} to be less sensitive to residual detuning during the tomography pulse.

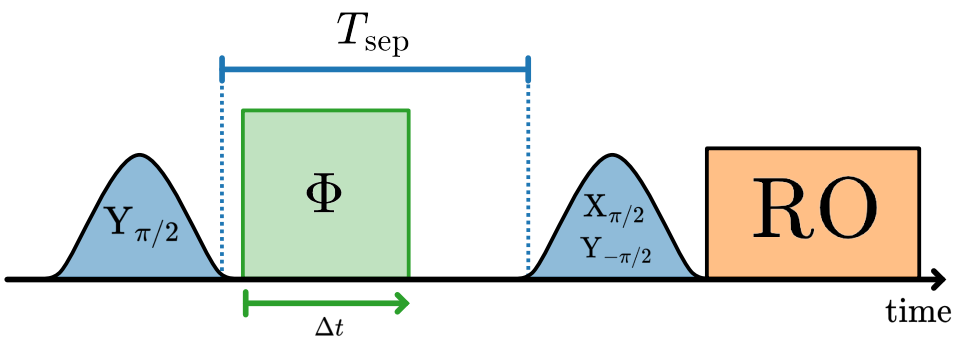

Figure 3.5: Cryoscope pulse sequence. The qubit is placed onto the equator with a $Y_{\pi/2}$ pulse and let rotate with a flux pulse Φ for a variable time Δt. After the flux pulse turns off, we wait until a time T_{sep} has passed since the initial $\pi/2$ pulse ended until we apply a tomography pulse to measure the qubits $\langle X\rangle$ and $\langle Y\rangle$ coordinates on the Bloch sphere. We wait 50 ns after applying the first $\pi/2$ pulse until we send the flux pulse and sweep Δt from zero to $T_{\text{sep}} - 50$ ns to give the qubit enough time to return to the flux insensitive point before the tomography pulse is applied.

The main advantage of the Cryoscope technique is that we can sample our flux pulse as finely as we can vary Δt, which means that the AWG generating the flux pulse is what limits the distortion timescales we can measure. In our case the AWG generating the flux pulse had 1 GHz sampling rate which allowed us to resolve distortion timescales down to 1 ns. Depending on the context, this can be a detriment since we need to sample the pulse with a short enough sampling time to capture the qubit rotation around the Z axis. In the language of the Nyquist theorem, this means that if our flux pulse detunes the qubit by Δf we need to sample the pulse with frequency $f_s = \Delta t^{-1} > 2\Delta f$. This also implies that we need some information

about the expected qubit detuning caused by the flux pulse. The simplest approach is to just set Δt equal to the AWG's limit and hope to capture the rotation.
The data extracted from a Cryoscope measurement is in the form of qubit $\langle X \rangle$ and $\langle Y \rangle$ values for a given flux pulse duration, Δt. These values are converted into accumulated qubit phase $\varphi = \arctan \frac{\langle Y \rangle}{\langle X \rangle}$ which is demodulated with the highest frequency component of the $\langle X \rangle$ and $\langle Y \rangle$ data before being unwrapped. This demodulation step removes the contribution of the target detuning to the rest of our analysis such that we can focus on the detuning caused only by distortions. The detuning due to the distortions are then estimated as $\Delta f = \frac{\partial \varphi}{\partial t}$, which was calculated using scipy's `savgol_filter` [58]. To estimate the total detuning, as the sum of the target detuning and the detuning from distortions, the highest frequency component of $\langle X \rangle$ and $\langle Y \rangle$ is added back to Δf.

3.4 TLS spectroscopy

As we saw in Section 2.5, a spectroscopical measurement of the qubit decay rate will show Lorentzian peaks when the qubit passes through resonance with a TLS. We can therefore measure TLSs by performing T_1 measurements of the qubit and fitting the qubit decay, which is the inverse of T_1, in frequency to Lorentzians, as given by Equation (2.21). A standard T_1 measurement takes some time, on the order of a minute. We want to minimise this time as TLSs are known to fluctuate in time [31]. To this end, we use the three-point method [59] to extract the qubit T_1 at each frequency step. This allows us to estimate the qubit decay time with only three measurements, as we discuss later in this subsection. The pulse scheme is shown in Figure 3.6. The qubit is excited and for a time Δt tuned to another frequency with a flux pulse Φ. The qubit population is then measured and an effective qubit decay rate estimated.

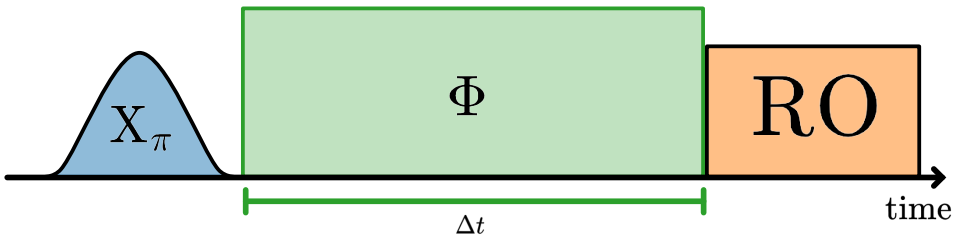

Figure 3.6: The sequence used to perform TLS spectroscopy. The qubit is initally excited with a π pulse and then tuned to another frequency with a flux pulse, Φ, for duration Δt. Afterwards, the qubit population is measured and an effective qubit decay rate estimated.

Let's assume that the qubit ground and excited states correspond to voltages $\mathcal{V}_0$ and $\mathcal{V}_1$, respectively. After decaying for time Δt, we measure the qubit population as a voltage $\mathcal{V}_s$. We assume that the qubit decays according to

$$\mathcal{V}(t) = Ae^{-t/T_1} + B, \tag{3.1}$$

where T_1 is the qubit decay time, and $\mathcal{V}(t)$ is the voltage we measure with the readout pulse after a time t. We know that $\mathcal{V}_0 = B$, and $\mathcal{V}_1 = A + B$, so we find that

$$T_1 = \frac{\Delta t}{\ln\left(\frac{\mathcal{V}_1 - \mathcal{V}_0}{\mathcal{V}_s - \mathcal{V}_0}\right)}, \tag{3.2}$$

is the estimated T_1 time using the three-point method. Since $\mathcal{V}_0$ and $\mathcal{V}_1$ do not change, we just need to measure them once and then sweep the qubit frequency by varying the amplitude of the flux pulse in Figure 3.6. In the supplementary material of [59] it was shown, using simulation, that the three-point method generally resulted in a factor two larger standard deviation compared to a full exponential measurement.

3.5 QP tunnelling

To measure QP tunnelling events we used a qubit that was weakly sensitive to offset charge. This was confirmed by performing repeated Ramsey measurements where the presence of two oscillating frequencies were measured, instead of just one. This measurement also gave us bounds for the rate of QP tunnelling events, if we had only seen one frequency of oscillation, a QP did not tunnel over the junction while we collected the trace. If a QP did tunnel, however, we would see two different frequencies of oscillation in the Ramsey trace. This is because the drive, f_d, will be detuned by $|f_d - f_{01}^{\text{even}}|$ and $|f_d - f_{01}^{\text{odd}}|$. The fact that we were able to measure sharp frequencies of oscillations, i.e. the Ramsey trace had two sharp peaks in the Fourier domain, means that the background charges change with a timescale slower than it takes to collect the Ramsey trace.

To measure single parity switching events, we first calibrated a parity-selective π pulse [37, 36], using the sequence shown in Figure 3.7. Initially, the qubit is placed on the equator with a $\pi/2$ pulse around the Y axis. Note that all pulses were sent at the average qubit transition frequency, so there should be no discrimination between even and odd parities. The qubit then rotates around the Z axis during a time $1/4\Delta f$, where $2\Delta f = |f_{01}^{\text{odd}} - f_{01}^{\text{even}}|$. Keep in mind that the qubit begins rotating during the XY pulses, which is why the waiting time is chosen as the start of the first XY pulse to the end of the last. From how we defined the even and odd transition frequencies in Figure 2.10, the even qubit state will rotate clockwise and the odd state counterclockwise.[3] In this case, a qubit in the even ground state will be mapped to the excited state and a qubit in the odd ground state will stay in the ground state after the second $\pi/2$ pulse is applied around the X axis.

[3] I use the left hand convention for state rotations around axis on the Bloch sphere, with the ground state at the North pole and the excited state at the South pole.

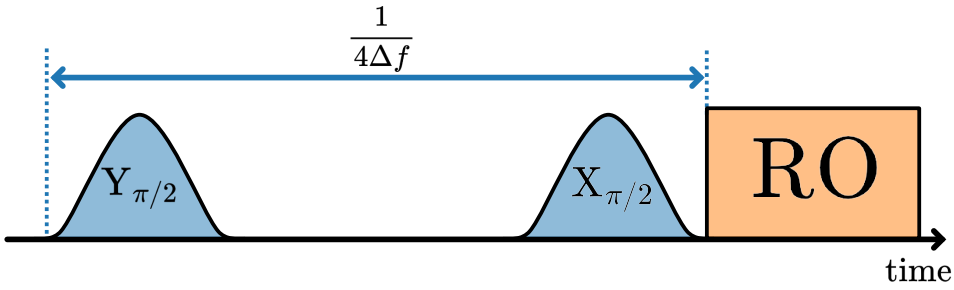

Figure 3.7: Pulse sequence of a parity selective π pulse. The $\pi/2$ pulses were sent at the average qubit frequency, f_{01}, and were 80 ns long. The spacing between them, $1/4\Delta f$ is chosen after performing a Ramsey measurement to find the current even and odd qubit transitions, where $2\Delta f = \left| f_{01}^{\text{odd}} - f_{01}^{\text{even}} \right|$.

We want to repeat the sequence of Figure 3.7 as fast as possible, since this will essentially sample the qubit parity in time, repeating the mapping faster will enable us to resolve the parity switches to a shorter timescale. We unfortunately do not have the luxury of qubit reset, which means that when our parity selective π pulse begins, the qubit might be in the ground state or the excited state. We find that given the different initial qubit states, it will be mapped to another state according to Table 3.2. In the even state, a qubit will keep switching between ground and excited, while a qubit in the odd state will remain in its initial state.

Table 3.2: Qubit state mapping depending on initial qubit state and whether it is odd or even. We see that the parity selective π pulse only rotates an even qubit state.

parity	initial qubit state	final qubit state
even	ground	excited
even	excited	ground
odd	ground	ground
odd	excited	excited

To sample the qubit parity in time, we repeat the sequence in time, as shown in Figure 3.8, and collect individual readout records with values zero or one. As we see in Table 3.2, the qubit will change its state only if the parity is even but remain in the same state if the parity is odd. We store the readout results in a vector of length N, $\mathbf{r} = \begin{pmatrix} \text{RO}_1 & \text{RO}_2 & \cdots & \text{RO}_N \end{pmatrix}$, and map them to the qubit parity according to

$$\mathbf{P} = 2|\Delta\mathbf{r}| - 1, \tag{3.3}$$

where $\mathbf{P}$ is the qubit parity at pairwise records, with length $N-1$, and $\Delta\mathbf{r}$ is the difference between pairwise readout values.

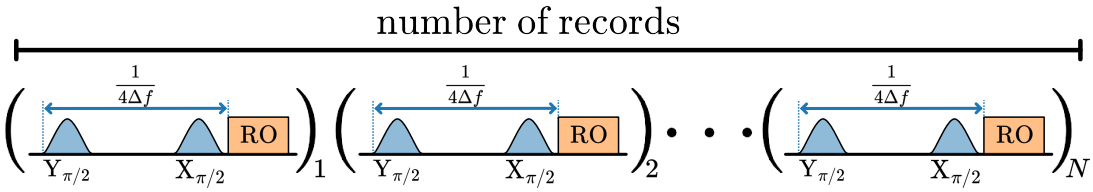

Figure 3.8: Pulse sequence for monitoring the qubit parity. Each parentheses contains a parity selective π pulse, followed by qubit state readout with output values zero or one, corresponding to the ground and excited state, respectively. To track the qubit parity we compare readout results from the current and previous record; if the qubit state changed the parity is even and if the state did not change, the parity is odd.

The number of records was usually on the order of 10k - 20k, and with each parity selective π pulse and readout taking 4 - 6 μs, our qubit parity was monitored for 40 - 120 ms. Before performing the sequence in Figure 3.8, a Ramsey measurement was taken to extract the *instantaneous* $2\Delta f$, which was found to vary on the timescale of minutes, and should therefore not influence the same waiting time chosen in each record of the $\sim$ 100s of milliseconds for the experiment in Figure 3.8.
We found the most success with measuring the qubit parity switching when applying a low power RO pulse. This is possibly because of measurement-induced state transitions [60, 61] and photons in the resonator that cause qubit dephasing [62]. If the resonator is not properly emptied before the next parity selective π pulse, the qubit will additionally decay, causing the parity mapping sequence to deteriorate. However, this was not rigorously studied during this thesis. Whether a RO pulse specifically designed to empty the resonator after readout would assist in measuring the qubit parity more accurately can also be tested [63].
For the results presented here, a Gaussian Naive Bayes classifier was used to discriminate between the qubit states [64], instead of Labber's SVC [65]. Generally, using a Naive Bayes classifier was more succesful, presumably due to poor discrimination between the two states. The state calibration for the results presented in this thesis is shown in Appendix C.

3.6 Purcell effect characterisation

To empirically measure the Purcell effect we measured the qubit T_1 time for the frequencies shown in Figure 3.3. We could tune the qubit through the resonator such that the detuning between the two could be swept from positive to negative values. To analyse our results we assume the contribution to our T_1 time to be from three different origins, TLSs (Section 2.5), QPs (Section 2.6) and the Purcell effect (Section 2.7). The ensembles of these three different processes contribute to the decay rate of the qubit

$$\Gamma_{\mathrm{Q}} = \Gamma_{\mathrm{TLS}} + \Gamma_{\mathrm{QP}} + \Gamma_p, \tag{3.4}$$

with Γ_{TLS}, Γ_{QP} and Γ_p the decay rate due to TLSs, QPs and the Purcell effect, respectively.

At millikelvin temperatures, and with qubit/resonator frequencies in the GHz regime, the TLS ensemble contributes with a decay rate of the form [50]

$$\Gamma_{\mathrm{TLS}} = f_q F \delta_{\mathrm{TLS}}, \tag{3.5}$$

where f_q is the qubit frequency, and the product $F\delta_{TLS}$ is a measure of how much loss the TLSs induce. The filling factor/participation ratio, F, describes the participation of the TLSs, and depends mostly on the geometry of the device. The TLS loss tangent is denoted by δ_{TLS}, and is a measure of how good the fabrication technique is. In this way, the product $F\delta_{\mathrm{TLS}}$ can be used as a figure of merit for how much the TLSs are contributing to the qubit decay rate [30].
The QP ensemble contributes with a decay rate given by [66, 67]

$$\Gamma_{\mathrm{QP}} = 2x_{\mathrm{QP}} f_q \sqrt{\frac{2\Delta_{sc}}{h f_q}}, \tag{3.6}$$

where Δ_{sc} is the superconducting gap parameter, and x_{QP} is the density of QPs normalised to the density of Cooper pairs [36].
Lastly, as mentioned previously, the Purcell effect will add a decay rate

$$\Gamma_p = \kappa \frac{C_g^2}{4C_q C_r} \frac{f_q f_r}{(f_q - f_r)^2}, \tag{3.7}$$

where f_r is the resonator frequency and the C's denote the various capacitances mentioned in Section 2.7.
We measure T_1 as a function of qubit frequency and fit the decay rate $\Gamma_{\mathrm{Q}} = 1/T_1$ to Equation (3.4) to see how accurate these models are. To compare our results to the single mode Purcell approximation we use our Γ_{Q} as a function of qubit frequency to extract an effective qubit resonator coupling rate. We then compare this to an independently measured coupling rate extracted from the dispersive shift as a function of qubit frequency. In Figure 3.9, we show the different measurements performed as two lanes, along with extracted parameters.
We fit Γ_{Q} as a function of qubit frequency to a modified Equation (3.4), given by

$$\Gamma_{\mathrm{Q}} = A \frac{f_q f_r}{(f_q - f_r)^2} + B f_q + C\sqrt{f_q}, \tag{3.8}$$

where the first term corresponds to the Purcell effect contribution, the second term the TLS contribution and the last term corresponds to the QP contribution. Immediately, we can extract some information about the TLSs and QPs. Indeed, comparing Equation (3.8) to Equations (3.5) and (3.6) we see that $B = F\delta_{\mathrm{TLS}}$ and $x_{\mathrm{QP}} = \frac{C}{2\sqrt{2\Delta_{sc}/h}}$, which tells us how much loss the TLSs contribute and what the ratio between broken and paired Cooper pairs is, respectively.
To see how accurate the Purcell model is, we need to go through more steps, and that is the main point of drawing the flow diagram in Figure 3.9. Essentially, we extract an effective coupling rate between the qubit and resonator from the Γ_{Q} as a function of qubit frequency measurement and compare it to the actual qubit-resonator coupling rate measured from the dispersive shift as a function of qubit frequency. In this way, we can see whether the single mode Purcell model is too restrictive or not restrictive enough.

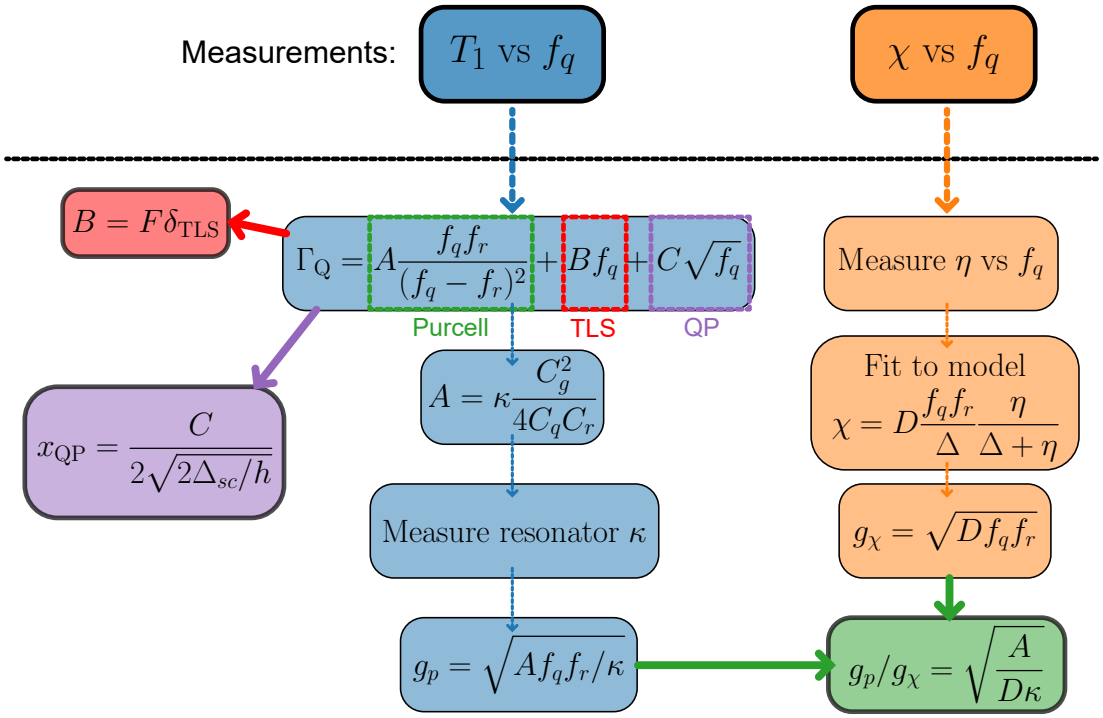

Figure 3.9: Flow diagram describing the steps performed in the Purcell characterisation experiment. The two lanes drawn in blue and orange show the measurements and parameter extractions needed. At the end of the two lanes we are able to determine whether the single mode Purcell approximation is valid or not. To the left of the blue lane we also depict the information we are able to extract about the TLSs and QPs in our device.

4
Results

In this chapter we put forth the results of the experiments discussed in Chapter 3, and discuss their implications by comparing them to similar work.

4.1 Flux pulse characterisation

We performed distortion measurements of the square flux pulses at the qubit flux-sensitive point, i.e. 0.25 Φ_0. Characterising flux pulses at 0.25 Φ_0 has the advantage of making the qubit maximally sensitive to distortions. At 0.25 Φ_0, the flux to qubit frequency transfer function is approximately linear, and second order terms are almost zero. This means that it is easier to single out the transfer function due to electrical components in the fridge without the complicated qubit transfer function of Figure 3.2 getting in the way. The flux pulse was applied with the qubit DC-biased at the flux-insensitive point, such that when the flux pulse was turned off, the qubit would only be very weakly susceptible to the turn off transients.
As we will discuss in Subsection 4.1.2, it was not possible to conduct the Cryoscope experiment at the flux-sensitive point.

4.1.1 Pulse wrapping

The sequence shown in Figure 3.4 essentially measures the step response of the flux pulse by using the qubit as an oscilloscope. The caveat is that our qubit oscilloscope only works when the qubit is susceptible to flux, namely *during* the flux pulse. Unless we would DC bias to a flux sensitive point, we are therefore not able to characterise the flux transients around the actual pulse.
In Figure 4.1 we show the main results of the pulse wrapping method. The blue points show the initial measured step response and the fit to the transfer function is the solid orange line. Knowing the transfer function which caused the distortion allows us invert it and apply the inverse to our flux pulse to predistort the pulse. The measured step response after predistorting the flux pulse is shown as green stars.
Normalising the reconstructed pulse of Figure 4.1 to the target, and fitting to the step response of Equation (2.17) we extract the step response parameters shown in Table 4.1. We find that the transfer function quickly overshoots the pulse with $\sim$ microsecond timescale and then slowly decays toward the target. In Figure 4.1 the slow decay might be difficult to see but additional measurements presented in Appendix D show that there is indeed an exponential decay toward the target after the overshoot.

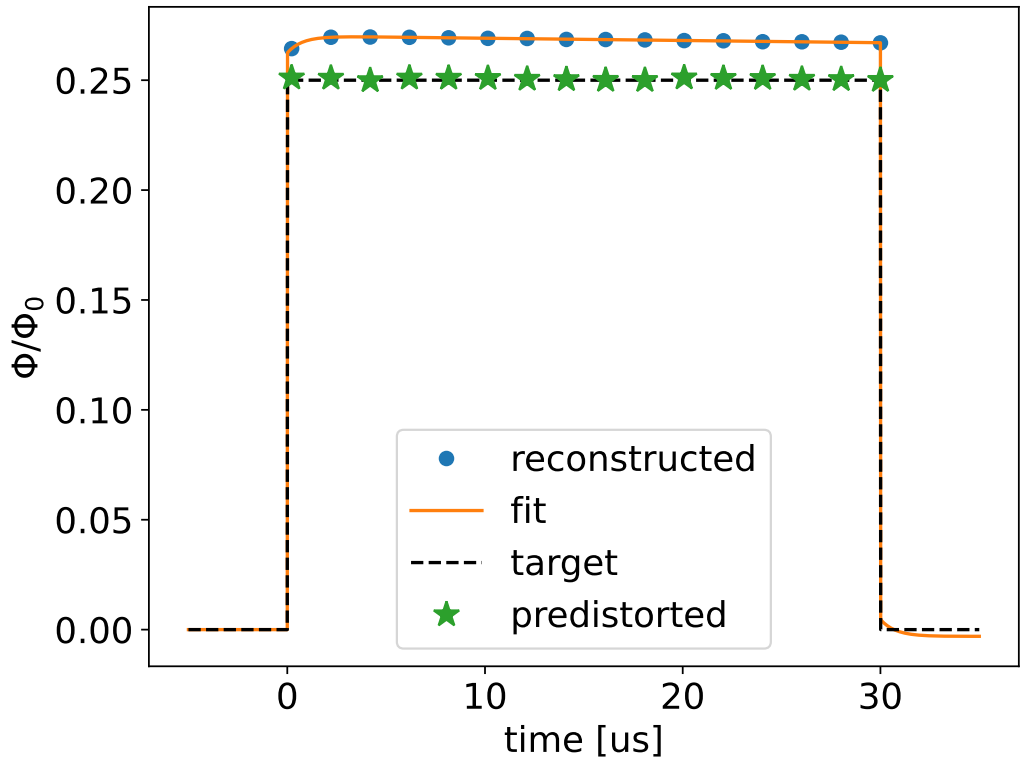

Figure 4.1: Square flux pulse distortions measured using the pulse wrapping method. The blue points show the initial reconstructed pulse and its fit to a transfer function is indicated with the solid orange line. Knowing the transfer function, we construct its inverse, apply it to our pulse, and measure the predistorted pulse shown as green stars. As a reference we show the target pulse as a dashed black line.

Room temperature measurements indicate that the fast overshoot is a remnant from the AWG, which is not adequately filtered away, or accentuated further when the fridge is cold. See Appendix E for room temperature measurement results. If the AWG does not cause the fast overshoot, it might be due to some on-chip effects, such as the qubit response.[1] The long distortion timescale has been attributed to the buildup of flux in the flux lines, in other work [27, 25]. It is possible to avoid the long timescale distortions by removing the DC component of the flux pulse, as done in [25].

Table 4.1: The systems step response parameters extracted by measuring a 30 μs square flux pulse at the flux-sensitive point.

a_0	τ_0	a_1	τ_1
$(-3.11 \pm 0.08) \cdot 10^{-2}$	760 ± 60 ns	$(8.08 \pm 0.02) \cdot 10^{-2}$	177 ± 5 μs

Using the parameters in Table 4.1 we construct the inverse IIR filter as described in Section 2.4.2, and digitise it using the bilinear transform. We then have a fractional form of the filter we want to apply to the pulse, and to actually apply it we use scipy's `lfilter` [68], and then feed the resulting pulse into our AWG. The result is the green stars in Figure 4.1 which have an average of (0.2506 ± 0.0004) Φ_0, with one standard deviation error of 0.2%. More detail on the filter implementation is shown in Appendix A.
Further characterisation of the flux pulse using the pulse wrapping method was not possible, as the temporal resolution of this method is limited by our spectroscopical pulse duration, which in our case is relatively long, being 200 ns. Trying to correct for the remaining 0.2% using an FIR filter did not turn out to be possible. After further predistortion, the 0.2% was simply replaced by some other form of distortion, or noise, indicating that we have corrected the pulse as much as possible.

4.1.2 Cryoscope

To study the rest of the 0.2% distortions present in the flux pulse we used the Cryoscope technique [24]. Even though we indicated that there is nothing left to correct for in the previous section, that is only true up to the 200 ns timescale available to us due to the spectroscopical pulse duration. Cryoscope, however, can sample the flux pulse equal to the AWG sampling time, which in our case is 1 ns. As mentioned in Section 3.3.2 we indirectly measure the flux pulse through the qubit by measuring the qubits acquired phase, by sampling the qubits rotation around the Z axis on the Bloch sphere. It just so turns out that the qubits flux-sensitive point is quite close to the digitiser's sampling rate (500 MS/s); from our calibration in Figure 3.2, we find that 0.25 Φ_0 corresponds to 493 MHz qubit frequency detuning from the sweetspot. This is why we chose to perform the Cryoscope measurement at lower flux threading the SQUID, targeting 0.1667 Φ_0, which corresponds to about 225 MHz detuning from the flux sweetspot.

[1] The qubit can be modelled as an RLC circuit and should therefore exhibit a second order step response.

In Figure 4.2 we summarise the result of the Cryoscope experiment, with our starting point being the predistorted pulse in Figure 4.1, shown as the blue line. Even though our initial distortion parameters were measured at the flux sensitive point, they are valid for the pulse amplitude in Figure 4.2, indicating agreement between the pulse wrapping and Cryoscope methods. Once the pulse was reconstructed, a least squares algorithm searched for the corresponding inverse transfer function $h_{\text{inv}}[n]$, such that applying the FIR filter cancelled out the original transfer function.

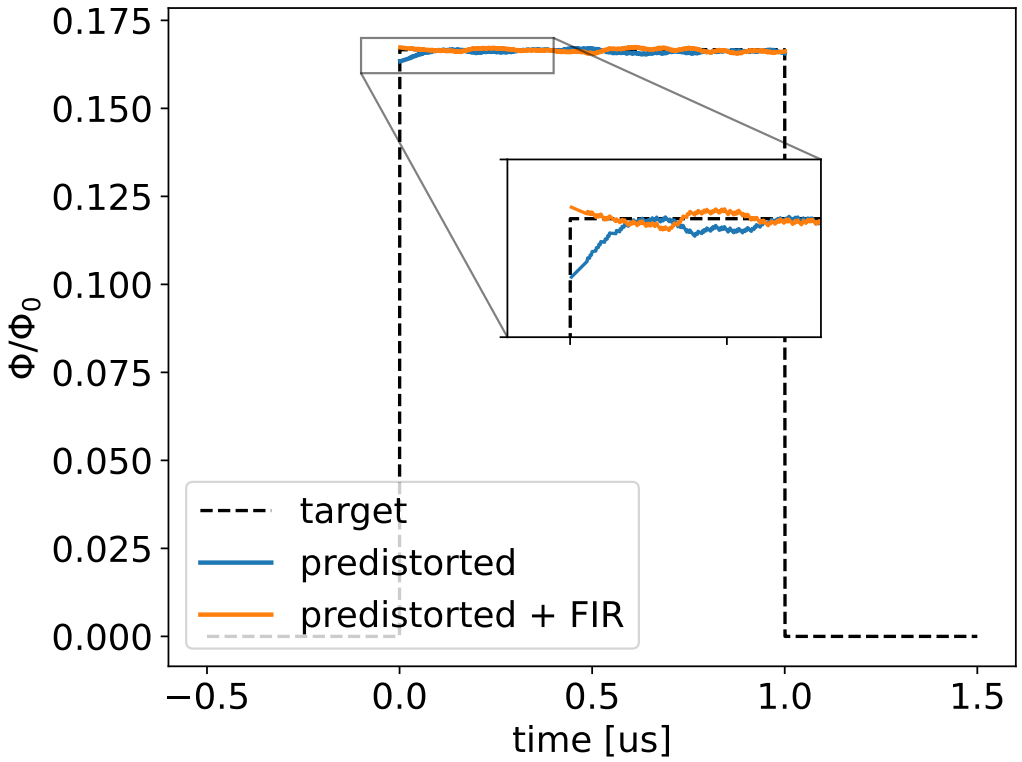

Figure 4.2: Reconstructed flux pulses measured using the Cryoscope technique. The initial pulse is shown as a solid blue line, and corresponds to a flux pulse predistorted using the pulse wrapping method. After reconstructing the pulse, an FIR filter was designed and applied to the pulse, with the final corrected pulse shown as a solid orange line. The inset shows how the short timescale rise is corrected for.

Comparing the orange and blue line in Figure 4.2 we find that the most significant result is the removal of an initial rise toward the target. Note that the timescale of this rise is less than 100 ns and would be difficult to characterise using the pulse wrapping method. We measured the initial predistorted pulse as mean $0.1661 \pm 0.0006\ \Phi_0$ and the FIR corrected pulse at mean $0.1665 \pm 0.0004\ \Phi_0$, which improves the error from 0.4% to 0.2% and has mean closer to the target $0.1667\ \Phi_0$.

The takeaway message from the Cryoscope results is that for long pulses on the order of tens of microseconds it is not feasible, nor necessary, to perform a Cryoscope experiment. When the flux pulse is shorter than, or on the order of one's calibrated π pulse, Cryoscope is a very powerful flux pulse characterisation technique.

4.2 TLS spectroscopy

Measuring the qubit decay rate as a function of qubit frequency results in data similar to the one shown in Figure 4.3, where the decay rate is shown with a solid blue line and peaks due to TLSs have been marked with orange crosses. The orange crosses show our initial guesses of which peaks correspond to TLSs, some of them will be thrown away at a later point if their fit is too poor. We took TLS spectroscopy traces for flux pulses with duration 10, 20 and 30 μs and found the one with the 10 μs to *look the best*. Looking the best, in this case, means having the most prominent TLS peaks, and a lower qubit decay rate floor. Indeed, a longer flux pulse will allow the qubit to interact with weaker coupled TLSs during the pulse, causing the decay floor to increase. Since many weakly coupled TLSs can interact with the qubit at the same time, they can shadow a strongly coupled TLS, making the strong TLS peak seem noisy.

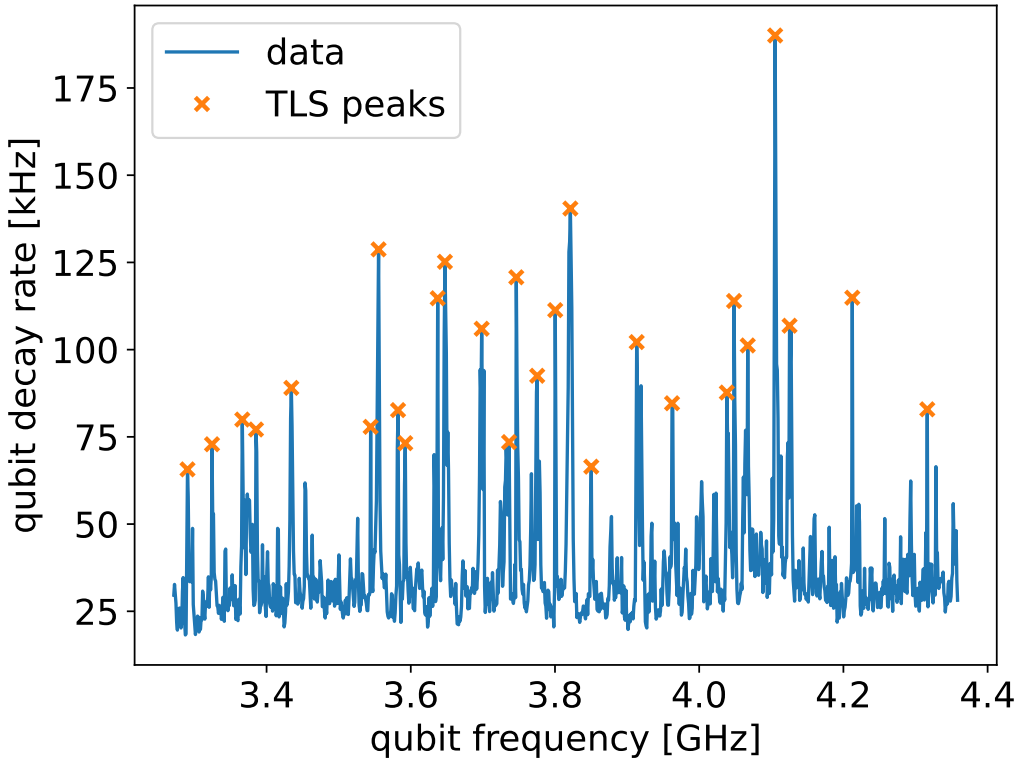

Figure 4.3: TLS spectroscopy measurement result showing the measured qubit decay rate with a solid blue line and peaks due to TLSs with orange crosses. The qubit frequency was swept with 1 MHz resolution. The flux pulse duration for this trace was 10 μs. Choosing which peaks correspond to TLSs and which peaks are simply noise can be quite subjective, and the crosses shown here are just one suggestion.

Once an initial guess for peaks corresponding to TLSs has been found, we try to fit each individual peak to its own Lorentzian, using the method presented in Appendix F. According to the model in Equation (2.21), the linewidth of the Lorentzian will give us information of the TLS and qubit decay rates, while the intensity will contain

information of both the TLS-qubit coupling rate and the TLS and qubit decay rates. As an example, we show the extracted TLS parameters from Figure 4.3 in Figure 4.4 where we plot the TLS decay rate as a function of the TLS-qubit coupling rate. We measure a lower bound for the TLS-qubit coupling rate as ~ 50 kHz, slightly above the coupling corresponding to the pulse duration $1/(2\pi\Delta t) \sim 16$ kHz. Coupling rates between 16 and 50 kHz are omitted due to the noise of the qubit decay rate. Furthermore, we only measure TLSs in the regime $g << \Gamma_{\mathrm{TLS}}$, and TLS peaks are only detectable if they have sufficient intensity, i.e. $2g^2/\Gamma > \mathcal{N}$, where $\mathcal{N}$ is what we define as the threshold for peak detection. This leads to another bound $\Gamma_{\mathrm{TLS}} < 4g^2/\mathcal{N} + \Gamma_{\mathrm{Q}}$, which is why this measurement method does not detect peaks in the top left of Figure 4.4, or the bottom right.

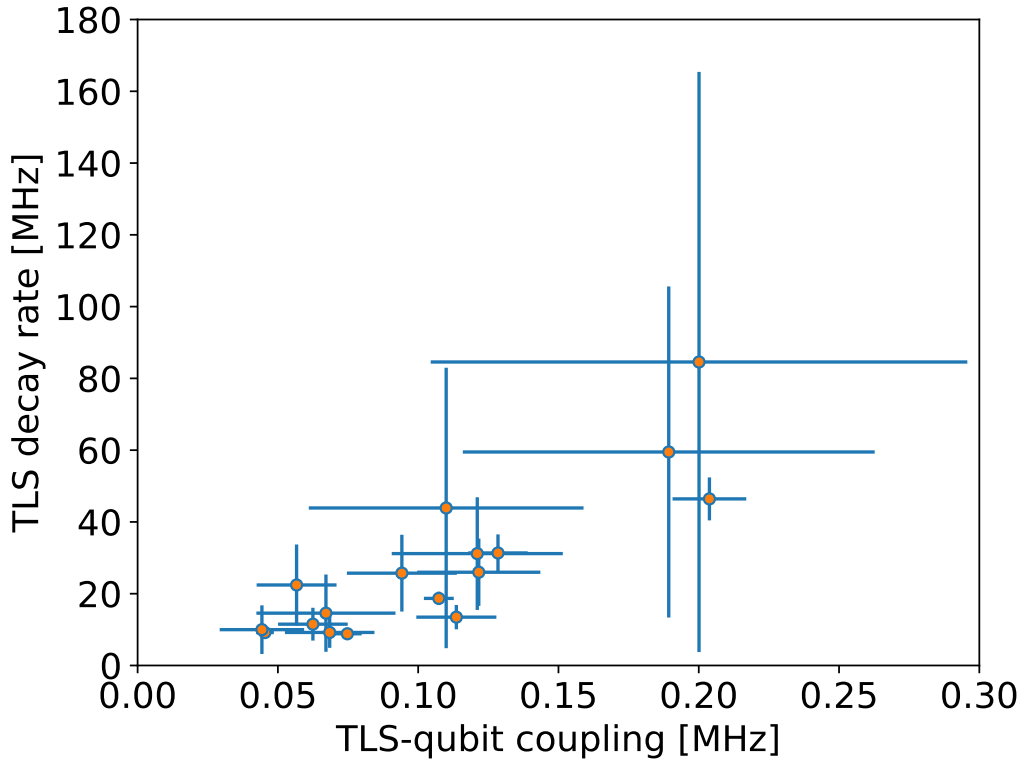

Figure 4.4: Example of measured TLS parameters shown as the TLS's decay rate as a function of its coupling rate to the qubit. The apparent trend where the TLS decay rate increases proportional to the TLS-qubit coupling, is not descriptive of the TLSs in our device and simply a result of the measurement technique.

It is known that TLSs fluctuate in time [31], presumably due to low frequency, thermally activated TLSs changing the higher frequency TLSs' frequency [9]. To this end, we repeat the trace in Figure 4.3 over 12 hours with an hour interval between each trace. The measured qubit decay rate is shown in Figure 4.5, where we observe switching between TLS frequencies with an hour timescale. We also find a very wide qubit peak moving between 3.8 to 4.2 GHz, a similar observation was made before [54], and was theorised to be a strongly-coupled TLS. The model described by Equation (2.21), states that a faster decaying TLS will increase the linewidth of the qubit decay rate around the TLS. This means that the TLS-qubit

coupling strength will need increase accordingly to fulfill $g << \Gamma_{\mathrm{TLS}}$. Comparing to other TLSs, the coupling of the wide TLS to the qubit was between 400 kHz to 600 kHz, with decay rate varying between 200 MHz to 500 MHz. In TLS measurements on phase qubits [69, 70] it was shown that TLSs in the JJ oxide couple to the qubit with rates on the order of 50 MHz, which is much stronger than the rates extracted here. It is not likely that the wide TLS measured resides in the oxide, indeed, it has been hypothesised that transmons *avoid* TLSs in the JJ oxide by relieving stress, which larger junctions are somehow unable to do [38].

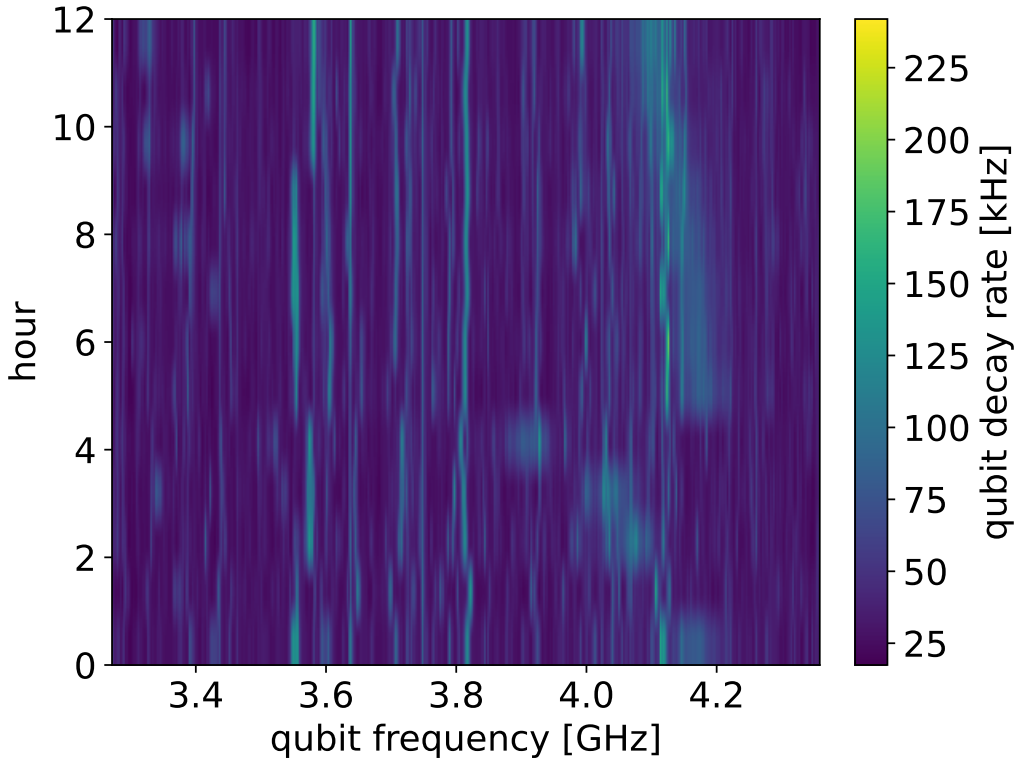

Figure 4.5: TLS spectroscopy repeated every hour for twelve hours. Switching of TLS frequencies with more than an hour timescale is apparent, as well as a wide, moving TLS at larger frequencies. Each qubit decay as a function of frequency trace took approximately 40 minutes.

Fitting each TLS spectroscopy trace in Figure 4.5 allows us to extract some statistics about the TLSs; the TLS density, coupling to qubit and TLS lifetime, as presented in Figure 4.6. We are able to fit ten to eighteen TLSs per GHz with less than a MHz coupling rate to the qubit and less than about 200 ns lifetime. The TLS-qubit coupling strengths above, and around 0.5 MHz are from the rapidly decaying TLS previously discussed. Compared to previous work in [54], the region of measured qubit-TLS coupling is larger in this work, with the TLS lifetime very similar. The TLS density (equal to the number of TLSs since the detuning range was chosen to be a GHz) is similar to the small-JJ qubits in [54], which had 14 and 29 measured TLSs. Note that when our TLS density is counted, the Lorentzians with poor fits have been omitted, so it's likely that the qubit measured in this project corresponds to the *Small-JJ Q2* in [54].

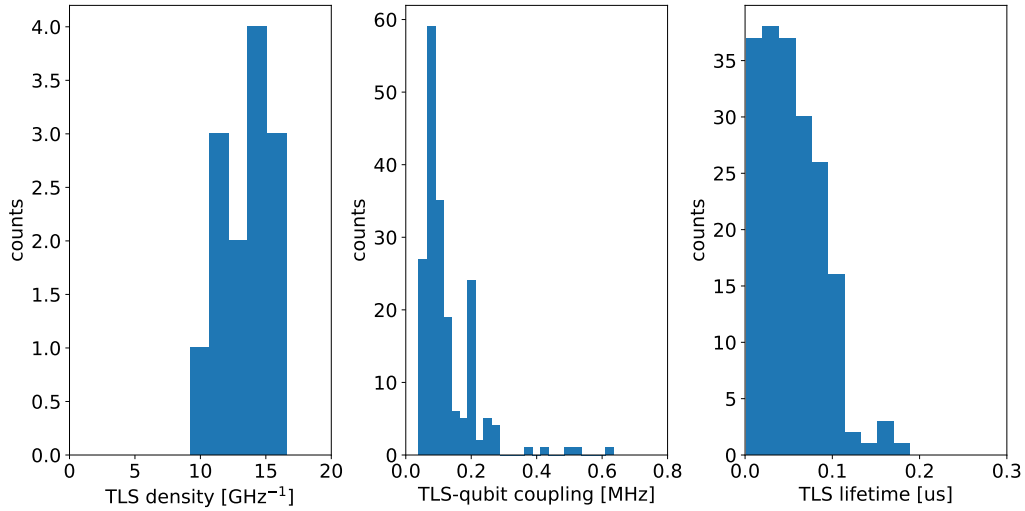

Figure 4.6: Extracted TLS parameters from a repeated TLS spectroscopy measurement. Ten to eighteen TLSs were observed per GHz, with coupling to qubit between 50 kHz and 650 kHz. The TLS lifetime shows a somewhat exponential decay in the number of observed TLSs as a function of TLS lifetime.

Regarding the error of these extracted TLS parameters, they are generally quite large. With 2k averages, the Lorentzian peaks are definitely not clean, as seen in Figure 4.3. From the calibration shown in Figure 3.2, we find that at the flux sensitive point we have $\frac{df_Q}{d\Phi} = 4.563 \frac{\mathrm{MHz}}{\mathrm{m}\Phi_0}$, which means that with fluctuations of flux on the order of $\mu\Phi_0$, our qubit frequency will fluctuate by ~ 4.5 kHz [71]. Note that the 0.2% flux pulse resolution we measure corresponds to about 500 $\mu\Phi_0$, which is considerably higher than low frequency flux noise measured in superconducting qubits [71, 72, 73], and only corresponds to about 2 MHz resolution of the qubit frequency tuning. To minimise the effect of magnetic field fluctuations, we could design a device with a larger SQUID loop or one which has less detuning range available. To decrease the voltage noise we could add additional attenuation to the flux line.

4.3 QP tunnelling

To measure individual qubit parity switches we needed information on the instantaneous detuning between the even and odd qubit states, since this will affect how long the waiting time between the $\pi/2$ pulses in Figure 3.7 is chosen. In Figure 4.7 we show the result of a repeated Ramsey experiment, where the two measured detunings are shown. The detunings were estimated by taking FFTs of individual Ramsey traces, and fitting the FFTs to two Lorentzians to determine the frequency components of the traces. The Ramsey experiments were repeated every minute in most cases. Notably, we find that the background charges drift, usually, with more than a minute timescale. The fact that two frequencies were measured with comparable intensity indicates that parity switching events are faster than the time it takes to collect the Ramsey traces, and the background charges move slower than

the time it takes to collect each trace.

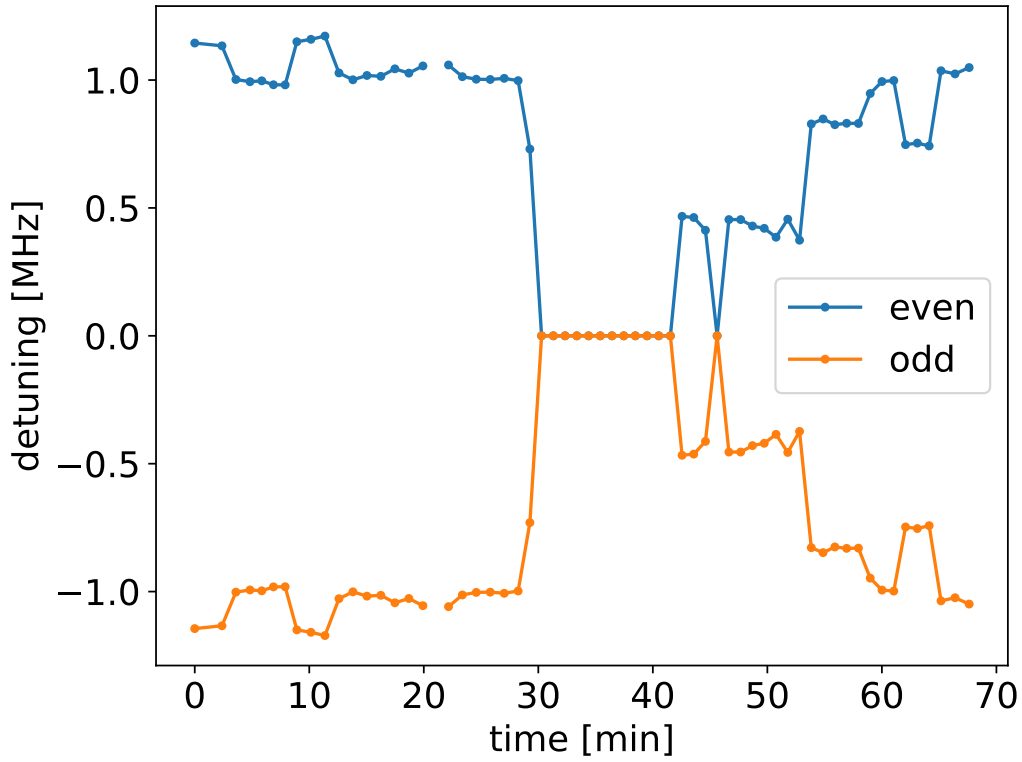

Figure 4.7: Temporal evolution of the even and odd qubit transition frequencies. As expected, they fluctuate symmetrically around the average qubit transition frequency, drawn as the zero on the y axis. Background charges cause the frequencies to drift with a timescale on the order of a minute. When both even and odd are on resonance, the qubit is at its charge-sensitive point.

After measuring the difference in frequency between the even and odd qubit states, we choose the waiting time of our parity-selective π pulse accordingly. For monitoring the parity, we chose to only perform the sequence shown in Figure 3.8 when the qubit was sufficiently close to the charge insensitive point. We set $2\Delta f > 2$ MHz as a threshold for the even-odd detuning. We measured the maximum detuning between the even and odd states as 2.34 MHz, in good agreement with numerical expectations.
A snapshot of one of the extracted parity traces is shown in Figure 4.8, where it is immediately clear that $P = -1$ is the preferential parity, and as discussed in Section 3.5, this corresponds to the qubit remaining in the same state between records. The average parity of the whole trace shown in Figure 4.8, which is ~ 72 ms long with 6 μs sampling time, was -0.44, indicating that our parity mapping scheme discriminates strongly between parities. Also note that the average qubit state was 0.45, which is quite close to the expected 0.5. For continuous monitoring of the qubit parity, a drive-dependent average parity has been reported in [55], whether this is also the case in our measurement is currently under investigation. The drive-dependent picture seems plausible if there is a difference in the parity switching rates when the qubit is excited or in the ground state. This was briefly investigated using a Hidden

Markov Model (HMM) and did show a difference in the even→odd and odd→even transition rates, but they were inconsistent with the rate extracted from the PSD. The HMM was very dependent on initial guesses for the model so it might not a very robust fitting technique, and ultimately requires more investigation.

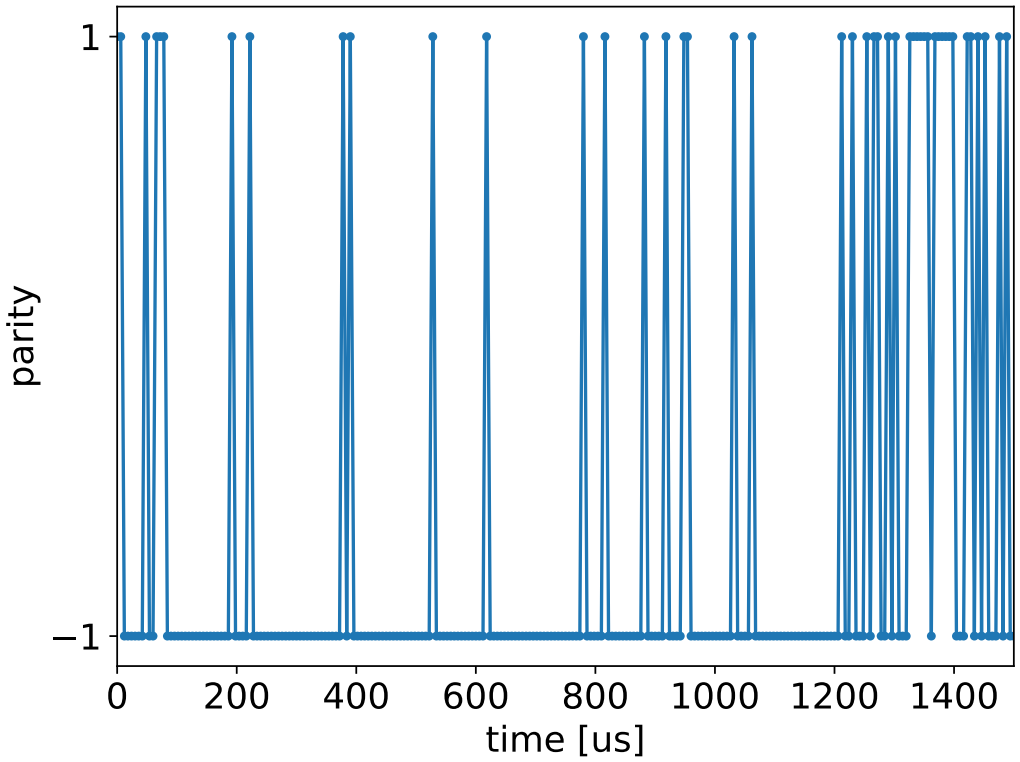

Figure 4.8: A 1.5 ms snapshot of a measurement of the qubit parity. The qubit remaining in the same state between single-shot readouts far outweighs the parity selective π pulse flipping the state. The qubit remaining in the same state between readouts corresponds to parity $P = -1$.

Qubit parity switches are modelled as a random telegraph switching (RTS) process, where the probability of remaining in the same parity is a decaying exponential as a function of time. The spectral density of such a correlated function is given by a Lorentzian [49, 36, 74]. To measure the spectral density, we took ten traces as the one in Figure 4.8, while making sure the detuning between even and odd states was sufficient, and fit their average spectral density to a Lorentzian, as shown in Figure 4.9. There will be uncorrelated errors due to the readout fidelity and the selective π pulse fidelity, which raise the offset floor of the spectral density [36, 75]. We fit our measured parity spectral density to a general Lorentzian

$$S(f) = \frac{A\Gamma}{\Gamma^2 + (\pi f)^2} + B, \tag{4.1}$$

where Γ is the corner frequency of the Lorentzian, corresponding to the qubit parity switching rate, and B encompasses white noise due to the parity sampling.

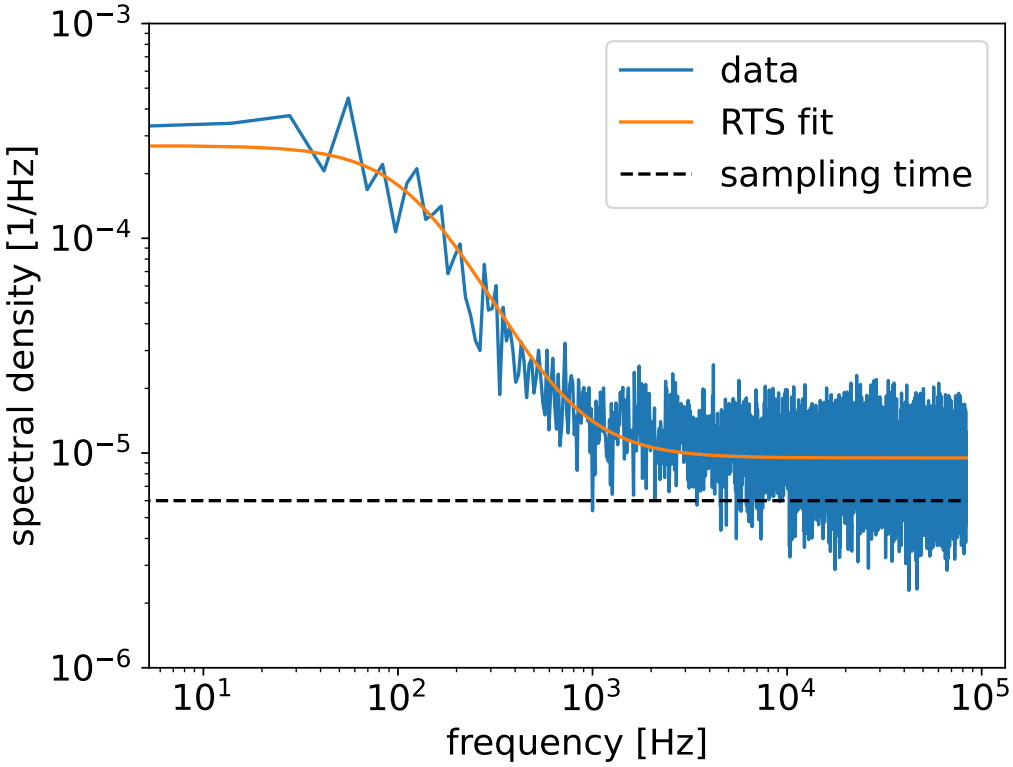

Figure 4.9: The average spectral density of ten independently measured qubit parity traces, each taking $\sim$ 72 ms. The data is fit to a Lorentzian with corner rolloff frequency $\Gamma = 421$ Hz. The dashed black line corresponds to a white noise floor at the sampling time of 6 μs, our RTS fit shows an offset higher than the sampling time indicating the presence of some additional noise.

The data used to generate Figure 4.9 had an average parity of the ten traces $\langle P \rangle = -0.4 \pm 0.3$, and a parity switching rate of $\Gamma = 421 \pm 7$ Hz. On its own, the parity switching rate does not have much meaning, and another measurement would be needed to correlate switching events with qubit decay [37], which would in turn allow us to estimate the number of broken Cooper pairs. This measurement might be planned for in the near future.
A group in the same division as my research group recently measured parity switching rate using direct detection, and found a much lower rate of $\sim$ 2.8 Hz [55]. We direct the reader to a nice summary of recently measured switching rates across multiple laboratories in the supplementary material of [55], where we see that our currently reported parity rate is not *state-of-the-art*. Whether this is due to insufficient shielding [76], or the qubit pad acting as an antenna for high frequency photons [77, 78] is unknown at this time. Note, however, that since we now have the ability of measuring the parity switching rate efficiently we can try to single out what is limiting it and how it can be decreased. One additional comment is perhaps that, as we reduce the parity switching rate, the lower frequency components of the spectral density become more important. To measure those, each trace should be measured for longer, i.e. with more single shots, and the trigger period can then in turn be increased as well, since the trigger period defines the maximum frequency we can measure. For some reason, the measurement software Labber was not able

to collect more than 12k single shots; it is still unclear whether this is due to the digitiser's memory limit, or some other issues.
To show the stability of our measured parity switching rate we repeated the measurement of Figure 4.9 every hour for 24 hours. In Figure 4.10 we show the result of this measurement, with the blue points showing the extracted parity switching rate and the orange stars showing the average parity of each trace. We find the switching rate to be relatively stable at 200 - 800 Hz, with small errors on each spectral density fit. The average parity is also seen to be stable between -0.25 to -0.5 with one standard deviation about 0.3.

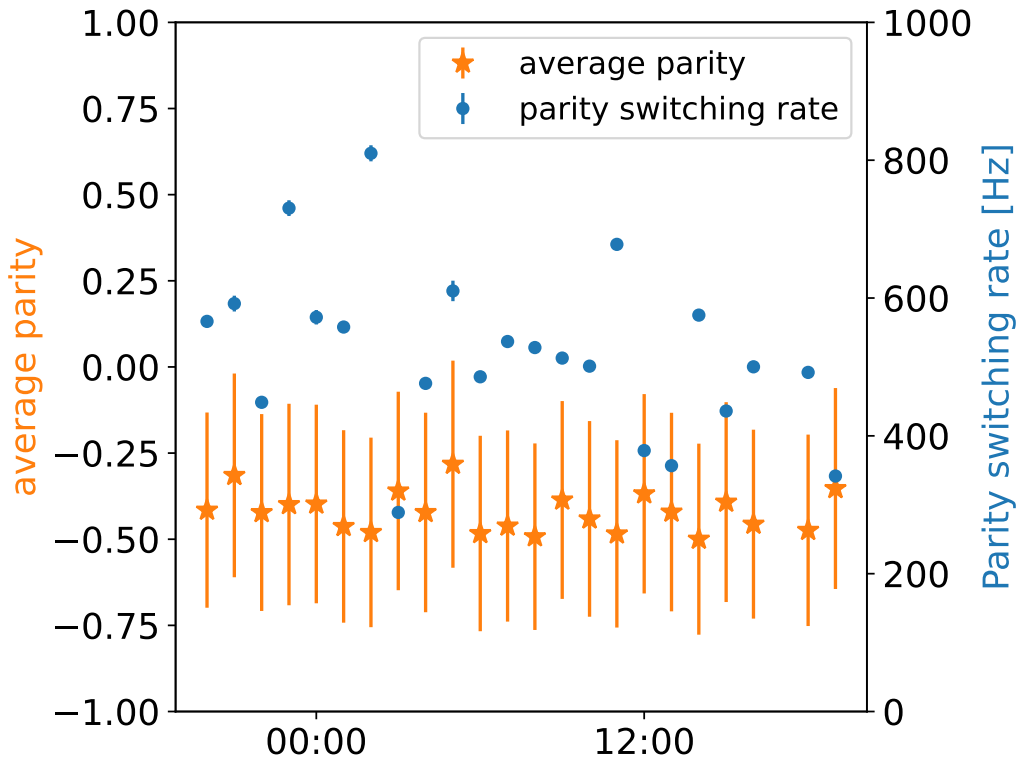

Figure 4.10: Results of measuring the qubit parity switching over 24 hours, repeated every hour. The left y-axis shows the parity scale and the right y-axis shows the scale of the parity switching rate. The parity switching rate is shown as blue points and the average parity of each trace is shown as orange stars.

4.4 Purcell effect

The point of performing what we have referred to as Purcell characterisation was to investigate whether the single mode approximation, given by Equation (2.23), was valid for our device. To this end, we measured the qubits relaxation time T_1 as a function of qubit frequency and fit to the model in Equation (3.8), as discussed in Section 3.6.
In Figure 4.11 we show the measured qubit decay rate as a function of qubit frequency. The blue and orange histograms depict the measured qubit decay rates, the legend labels which date they were measured. The blue data was averaged 100x over a couple of hours and the orange data, taken a day later, was averaged 50x over almost twenty hours. The solid curves show the contributions of different origin, and the dashed black line shows the total qubit relaxation rate as the sum of the colored curves.

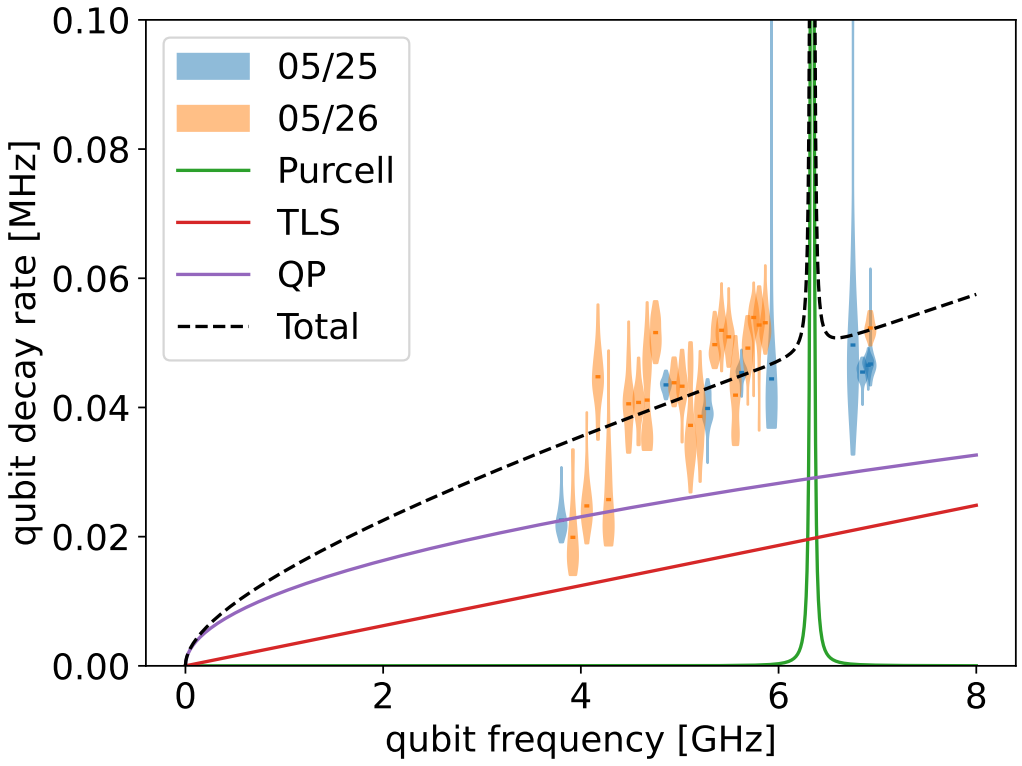

Figure 4.11: Qubit relaxation rate as a function of qubit frequency. Blue and orange histograms show measurement results from 100 and 50 T_1 measurements, respectively, converted to decay rate. Green, red and purple solid lines depict the contribution of the Purcell effect, TLSs and QPs, respectively. The total qubit decay rate fit is shown as a dashed black line.

The model, given by Equation (3.8), turns out to be too complicated for the data in Figure 4.11. The Purcell effect contribution dominates when the qubit and resonator are close to resonance but in that regime, the detuning is very small and we exit the dispersive regime. When trying to drive the qubit we also drive the resonator, and there can be direct energy exchange between the two, so any kind of measurement on

the qubit is very difficult. As the qubit and resonator become more detuned, another problem arises; the dispersive shift becomes too small. Indeed, the dispersive shift roughly scales as $\sim g^2/\Delta$, so when the detuning becomes large the dispersive shift becomes smaller and discriminating between the two qubit states becomes difficult. This method of characterising each contribution to the decay is not very useful, since we can not measure the regimes where individual contributions dominate.
Despite these problems, we still go through with the rest of the analysis and try to at least find some bounds for the different relaxation contributions. In Table 4.2 we show the optimal fitting parameters with their standard deviation, and the parameters we extract. Due to the limited qubit frequency range measured in Figure 4.11, the optimal fit of Equation (3.8) sets the Purcell contribution to the qubit decay as zero, with some standard deviation.

Table 4.2: Extracted parameters of the relaxation contributions of the Purcell effect, TLSs and QPs. In the rightmost column we indicate what the measurement result implies for the Purcell model, the TLS participation ratio and the QP density. The Purcell result shows how the single mode approximation should be scaled to coincide with our measurement result.

Origin	Fitting parameter	Physical result
Purcell	$A \in [0, 5 \cdot 10^{-6}]$	$\left(\frac{g_p}{g_\chi}\right)^2 \in [0, 0.06]$
TLS	$B = (3 \pm 1) \cdot 10^{-6}$	$F\delta_{\text{TLS}} = (3 \pm 1) \cdot 10^{-6}$
QP	$C = (1.2 \pm 0.2) \cdot 10^{-2} \frac{\text{MHz}}{\sqrt{\text{GHz}}}$	$x_{\text{QP}} = (6 \pm 1) \cdot 10^{-7}$

As shown in Table 4.2, the ratio g_p^2/g_χ^2, which was presented in Subsection 3.6, Figure 3.9, was less than one. This implies that the single mode Purcell approximation is too restrictive, and for our results to be consistent with the model, the model should be scaled by 0 to 0.06.
The extracted TLS participation ratio was found to be $(3 \pm 1 \cdot 10^{-6})$, which is of a similar magnitude to the films recently measured in [30], even if on the higher end. It should not be surprising that the TLS participation ratio is higher, since our device has a qubit and a flux line, contrary to [30]. This means there are additional substrate-air interfaces, and while they might not be the limiting interfaces, they will still contribute to increase losses.
Lastly, we can also extract the density of broken Cooper pairs normalised to the density of Cooper pairs, which we find to be $x_{\text{QP}} = (6 \pm 1) \cdot 10^{-7}$. In thermal equilibrium, the QP density can be estimated as [36]

$$x_{\text{QP}} = \sqrt{\frac{2\pi T}{\Delta_{sc}}} e^{-\Delta_{sc}/T}, \tag{4.2}$$

where T is the qubit temperature and Δ_{sc} the superconducting gap. Solving Equation (4.2) for an effective temperature, we find that the QP density in Table 4.2 corresponds to a qubit temperature of $T_{\text{eff}} = 147 \pm 2$ mK. Since our device is cooled to 10 mK, this reinstates the fact that QPs are not in thermal equilibrium, as has been previously reported [36, 37, 55].

Ultimately, our experiment states that the Purcell effect is negligible compared to the TLS and QP contributions for most qubit-resonator detunings, which we normally choose as about 2 GHz with the qubit well below the resonator. As an estimate, we can say that with a qubit-resonator coupling $g \sim 100$ MHz, which is larger than we measured, and with a resonator linewidth $\kappa \sim 550$ kHz, the Purcell effect with 2 GHz detuning would limit the qubit T_1 to just below 1 ms; about an order of magnitude greater than the maximum we measure in Figure 4.11. Another method of seeing the Purcell effect more clearly would be to limit the TLS participation to the qubit decay by not applying a DC offset flux offset to tune the qubit frequency, but to instead apply a short flux pulse; essentially performing TLS spectroscopy over a wide qubit frequency range. This might assist in making the Purcell effect more clear from the experiment, but is yet to be tested. Indeed, there are other problems that arise when using flux pulses instead of DC offset, such as pulse distortion. The device might also need to be redesigned, since at the flux-insensitive point, the detuning between qubit and resonator is very small, only on the order of 500 MHz. This was partly due to the qubit having significantly lower maximum frequency than designed, about 500 MHz, but should mostly be attributed to a mistake in the design.

5
Conclusion

In this thesis we have described experimental methods for characterising the environment which interacts with superconducting qubits. First, we described how to measure square flux pulse distortions and how to correct for them using two different qubit measurement techniques. The flux pulse distortions can be used to benchmark flux line designs, as done in [56]. With accurate flux pulse characterisation we showed how to perform TLS spectroscopy to measure the presence of strongly coupled TLSs, which decay much faster than they interact with the qubit. This measurement technique can be used to monitor how design changes, such as the ones made in [30], affect the TLS environment surrounding the qubit. In [30], it was noted that increasing the aluminium film thickness decreased the participation ratio of TLSs. One would also expect thicker films to distribute the electric field over more volume, which might decrease the coupling strength between qubit and TLS [79]. The density of TLSs can also be used as a figure of merit between fabrication processes [80], if a sufficiently large frequency range can be measured. The measurement we presented to analyse TLSs requires a frequency tunable qubit, which is not the type of qubit my group is focused on researching. There is another method of measuring TLSs via the AC Stark shift [81], and this might be interesting to try since it is readily available in our devices.

Quasiparticles cause the qubit parity to change by electrons tunnelling over the junction. We have described how to measure the rate of this parity switching using a parity selective π pulse. The number of quasiparticles in ones device is heavily influenced both by device shielding [76] and the qubit design [77, 78, 75, 82, 83]. The parity switching rate can be used as a figure of merit for both cases, since parity switches are directly related to qubit decoherence. More or fewer quasiparticles will increase or decrease the parity switching rate, respectively.

The TLS and quasiparticle ensembles, as well as the Purcell effect, are the three main contributors to the qubit decoherence rate [50]. By measuring the qubit decay rate as a function of qubit frequency, we tried to investigate whether the single mode Purcell approximation is valid [49]. This study was inconclusive, as it was too difficult to measure the different dominating regimes all on the same qubit-resonator system. In any case, we have at least described the idea behind such a measurement, avenues for improving the results include more averages and perhaps flux pulses, instead of DC offsets. A more careful design of the device might also be necessary. Directly measuring the Purcell effect with a DC flux offset would always be difficult since the qubit-resonator detuning needs to be small for the effect to be dominating. To stay in the dispersive regime, $g/\Delta << 1$, the coupling between qubit and resonator also needs to be made small. One can imagine that decreasing the coupling between

qubit and resonator would increase the duration of our readout and also increase the environments effect, since the coupling to resonator and environment become comparable. To measure larger qubit-resonator detunings the opposite becomes true, we should increase the coupling between qubit and resonator even further, such that the dispersive shift g^2/Δ does not become too small at these large detunings. Understanding how the environment interacts with superconducting qubits is imperative to the field's advancement. In this thesis we have discussed measurement techniques for analysing different components of the environment which the qubit couples to. Changes in fabrication, design and shielding should not only be motivated by changes in the qubit coherence, but also by noting how the qubit alters its interaction with the environment or how the environment is affected. In this way, we move the technology forward on a first principle basis, understanding why each change is made.

Bibliography

[1] Riccardo Manenti and Mario Motta. *Quantum Information Science*. Oxford University Press, 198 Madison Avenue, New York, NY 10016, United States of America, 2023.

[2] Claude Cohen-Tannoudji, Bernard Diu, and Franck Laloë. *Quantum Mechanics, Volume 1*. WILEY-VCH Verlag GmbH and Co., Boscstr. 12, 69469 Weinheim, Germany, 2020.

[3] David P. DiVincenzo. The physical implementation of quantum computation. *Fortschritte der Physik*, 48(9–11):771–783, September 2000.

[4] Alexandre Blais, Arne L. Grimsmo, S. M. Girvin, and Andreas Wallraff. Circuit quantum electrodynamics. *Reviews of Modern Physics*, 93(2), May 2021.

[5] P. Krantz, M. Kjaergaard, F. Yan, T. P. Orlando, S. Gustavsson, and W. D. Oliver. A quantum engineer's guide to superconducting qubits. *Applied Physics Reviews*, 6(2), June 2019.

[6] R. J. Schoelkopf and S. M. Girvin. Wiring up quantum systems. *Nature*, 451(7179):664–669, February 2008.

[7] Amr Osman. Reliability and reproducibility of josephson junction fabrication-steps towards an optimized process. 2019.

[8] Seong Hyeon Park, Gahyun Choi, Gyunghun Kim, Jaehyeong Jo, Bumsung Lee, Geonyoung Kim, Kibog Park, Yong-Ho Lee, and Seungyong Hahn. Characterization of broadband purcell filters with compact footprint for fast multiplexed superconducting qubit readout. *Applied Physics Letters*, 124(4), January 2024.

[9] Clemens Müller, Jared H Cole, and Jürgen Lisenfeld. Towards understanding two-level-systems in amorphous solids: insights from quantum circuits. *Reports on Progress in Physics*, 82(12):124501, October 2019.

[10] Leonid Glazman and Gianluigi Catelani. Bogoliubov quasiparticles in superconducting qubits. *SciPost Physics Lecture Notes*, June 2021.

[11] Samantha Buck, Robin Coleman, and Hayk Sargsyan. Continuous variable quantum algorithms: an introduction, 2021.

[12] Axel M. Eriksson, Théo Sépulcre, Mikael Kervinen, Timo Hillmann, Marina Kudra, Simon Dupouy, Yong Lu, Maryam Khanahmadi, Jiaying Yang, Claudia Castillo Moreno, Per Delsing, and Simone Gasparinetti. Universal control of a bosonic mode via drive-activated native cubic interactions, 2023.

[13] Marina Kudra, Mikael Kervinen, Ingrid Strandberg, Shahnawaz Ahmed, Marco Scigliuzzo, Amr Osman, Daniel Pérez Lozano, Mats O. Tholén, Riccardo Borgani, David B. Haviland, Giulia Ferrini, Jonas Bylander, Anton Frisk Kockum, Fernando Quijandría, Per Delsing, and Simone Gasparinetti. Robust prepa-

ration of wigner-negative states with optimized snap-displacement sequences. *PRX Quantum*, 3:030301, Jul 2022.

[14] U. Réglade, A. Bocquet, R. Gautier, J. Cohen, A. Marquet, E. Albertinale, N. Pankratova, M. Hallén, F. Rautschke, L.-A. Sellem, P. Rouchon, A. Sarlette, M. Mirrahimi, P. Campagne-Ibarcq, R. Lescanne, S. Jezouin, and Z. Leghtas. Quantum control of a cat qubit with bit-flip times exceeding ten seconds. *Nature*, 629(8013):778–783, May 2024.

[15] J.R Waldram. *Superconductivity of Metals and Cuprates*. CRC Press, December 2017.

[16] Uri Vool and Michel Devoret. Introduction to quantum electromagnetic circuits. *International Journal of Circuit Theory and Applications*, 45(7):897–934, June 2017.

[17] Jens Koch, Terri M. Yu, Jay Gambetta, A. A. Houck, D. I. Schuster, J. Majer, Alexandre Blais, M. H. Devoret, S. M. Girvin, and R. J. Schoelkopf. Charge-insensitive qubit design derived from the cooper pair box. *Physical Review A*, 76(4), October 2007.

[18] J Rahamim. *Development of a coaxial circuit QED architecture for quantum computing*. PhD thesis, University of Oxford, 2019.

[19] Y. Nakamura, Yu. A. Pashkin, and J. S. Tsai. Coherent control of macroscopic quantum states in a single-cooper-pair box. *Nature*, 398(6730):786–788, April 1999.

[20] Miguel Orszag. *Atom–Field Interaction*, page 99–113. Springer International Publishing, 2016.

[21] O. Astafiev, A. M. Zagoskin, A. A. Abdumalikov, Yu. A. Pashkin, T. Yamamoto, K. Inomata, Y. Nakamura, and J. S. Tsai. Resonance fluorescence of a single artificial atom. *Science*, 327(5967):840–843, February 2010.

[22] Tae Hong Park. *Introduction To Digital Signal Processing : Computer Musically Speaking.* World Scientific Publishing Company, 2009.

[23] Richard G. Lyons. *Understanding digital signal processing.* Prentice Hall PIR, 2004.

[24] M. A. Rol, L. Ciorciaro, F. K. Malinowski, B. M. Tarasinski, R. E. Sagastizabal, C. C. Bultink, Y. Salathe, N. Haandbaek, J. Sedivy, and L. DiCarlo. Time-domain characterization and correction of on-chip distortion of control pulses in a quantum processor. *Applied Physics Letters*, 116(5), February 2020.

[25] M. A. Rol, F. Battistel, F. K. Malinowski, C. C. Bultink, B. M. Tarasinski, R. Vollmer, N. Haider, N. Muthusubramanian, A. Bruno, B. M. Terhal, and L. DiCarlo. Fast, high-fidelity conditional-phase gate exploiting leakage interference in weakly anharmonic superconducting qubits. *Phys. Rev. Lett.*, 123:120502, Sep 2019.

[26] V. Negîrneac, H. Ali, N. Muthusubramanian, F. Battistel, R. Sagastizabal, M. S. Moreira, J. F. Marques, W. J. Vlothuizen, M. Beekman, C. Zachariadis, N. Haider, A. Bruno, and L. DiCarlo. High-fidelity controlled-z gate with maximal intermediate leakage operating at the speed limit in a superconducting quantum processor. *Phys. Rev. Lett.*, 126:220502, Jun 2021.

[27] Sebastian Krinner, Nathan Lacroix, Ants Remm, Agustin Di Paolo, Elie Genois, Catherine Leroux, Christoph Hellings, Stefania Lazar, Francois Swiadek, Jo-

hannes Herrmann, Graham J. Norris, Christian Kraglund Andersen, Markus Müller, Alexandre Blais, Christopher Eichler, and Andreas Wallraff. Realizing repeated quantum error correction in a distance-three surface code. *Nature*, 605(7911):669–674, May 2022.

[28] Muhammad Nasir Khan. *Electronic Signals and Systems : Analysis, Design and Applications.* River Publishers, 2020.

[29] Jonas Butscher. Shaping of fast flux pulses for two-qubit gates. Master's thesis, ETH Zürich, 2018.

[30] Janka Biznárová, Amr Osman, Emil Rehnman, Lert Chayanun, Christian Križan, Per Malmberg, Marcus Rommel, Christopher Warren, Per Delsing, August Yurgens, Jonas Bylander, and Anita Fadavi Roudsari. Mitigation of interfacial dielectric loss in aluminum-on-silicon superconducting qubits, 2023.

[31] P. V. Klimov, J. Kelly, Z. Chen, M. Neeley, A. Megrant, B. Burkett, R. Barends, K. Arya, B. Chiaro, Yu Chen, A. Dunsworth, A. Fowler, B. Foxen, C. Gidney, M. Giustina, R. Graff, T. Huang, E. Jeffrey, Erik Lucero, J. Y. Mutus, O. Naaman, C. Neill, C. Quintana, P. Roushan, Daniel Sank, A. Vainsencher, J. Wenner, T. C. White, S. Boixo, R. Babbush, V. N. Smelyanskiy, H. Neven, and John M. Martinis. Fluctuations of energy-relaxation times in superconducting qubits. *Phys. Rev. Lett.*, 121:090502, Aug 2018.

[32] Clemens Müller, Jürgen Lisenfeld, Alexander Shnirman, and Stefano Poletto. Interacting two-level defects as sources of fluctuating high-frequency noise in superconducting circuits. *Phys. Rev. B*, 92:035442, Jul 2015.

[33] Nimrod Moiseyev. *Non-Hermitian Quantum Mechanics*. Cambridge University Press, 2011.

[34] Carl M Bender. Making sense of non-hermitian hamiltonians. *Reports on Progress in Physics*, 70(6):947–1018, May 2007.

[35] Theodore Van Duzer, C. W. Turner, Donald G. McDonald, and Alan F. Clark. Principles of superconductive devices and circuits. 1981.

[36] D. Ristè, C. C. Bultink, M. J. Tiggelman, R. N. Schouten, K. W. Lehnert, and L. DiCarlo. Millisecond charge-parity fluctuations and induced decoherence in a superconducting transmon qubit. *Nature Communications*, 4(1), May 2013.

[37] K. Serniak, M. Hays, G. de Lange, S. Diamond, S. Shankar, L. D. Burkhart, L. Frunzio, M. Houzet, and M. H. Devoret. Hot nonequilibrium quasiparticles in transmon qubits. *Phys. Rev. Lett.*, 121:157701, Oct 2018.

[38] John M. Martinis and A. Megrant. Ucsb final report for the csq program: Review of decoherence and materials physics for superconducting qubits, 2014.

[39] John M. Martinis, M. Ansmann, and J. Aumentado. Energy decay in josephson qubits from non-equilibrium quasiparticles, 2009.

[40] G. Catelani, S. E. Nigg, S. M. Girvin, R. J. Schoelkopf, and L. I. Glazman. Decoherence of superconducting qubits caused by quasiparticle tunneling. *Phys. Rev. B*, 86:184514, Nov 2012.

[41] G. Catelani, J. Koch, L. Frunzio, R. J. Schoelkopf, M. H. Devoret, and L. I. Glazman. Quasiparticle relaxation of superconducting qubits in the presence of flux. *Phys. Rev. Lett.*, 106:077002, Feb 2011.

[42] M. Houzet, K. Serniak, G. Catelani, M. H. Devoret, and L. I. Glazman. Photon-assisted charge-parity jumps in a superconducting qubit. *Phys. Rev. Lett.*, 123:107704, Sep 2019.

[43] Gianluigi Catelani. Quasiparticles in superconducting qubits: History and recent developments. Online seminar, April 2021. Hosted by Zlatko Minev. Accessed: 2024-06-03.

[44] Thomas Connolly, Pavel D. Kurilovich, Spencer Diamond, Heekun Nho, Charlotte G. L. Bøttcher, Leonid I. Glazman, Valla Fatemi, and Michel H. Devoret. Coexistence of nonequilibrium density and equilibrium energy distribution of quasiparticles in a superconducting qubit. *Phys. Rev. Lett.*, 132:217001, May 2024.

[45] Mikhail V. Rybin, Sergei F. Mingaleev, Mikhail F. Limonov, and Yuri S. Kivshar. Purcell effect and lamb shift as interference phenomena. *Scientific Reports*, 6(1), February 2016.

[46] E. M. Purcell, H. C. Torrey, and R. V. Pound. Resonance absorption by nuclear magnetic moments in a solid. *Phys. Rev.*, 69:37–38, Jan 1946.

[47] Alexandre Blais, Ren-Shou Huang, Andreas Wallraff, S. M. Girvin, and R. J. Schoelkopf. Cavity quantum electrodynamics for superconducting electrical circuits: An architecture for quantum computation. *Phys. Rev. A*, 69:062320, Jun 2004.

[48] Eyob A. Sete, John M. Martinis, and Alexander N. Korotkov. Quantum theory of a bandpass purcell filter for qubit readout. *Phys. Rev. A*, 92:012325, Jul 2015.

[49] A. A. Houck, J. A. Schreier, B. R. Johnson, J. M. Chow, Jens Koch, J. M. Gambetta, D. I. Schuster, L. Frunzio, M. H. Devoret, S. M. Girvin, and R. J. Schoelkopf. Controlling the spontaneous emission of a superconducting transmon qubit. *Phys. Rev. Lett.*, 101:080502, Aug 2008.

[50] Andreas Bengtsson. *Quantum information processing with tunable and low-loss superconducting circuits*. PhD thesis, Chalmers, Microtechnology and Nanoscience (MC2), 2020.

[51] Bluefors. LD. `https://bluefors.com/products/dilution-refrigerator-measurement-systems/ld-dilution-refrigerator-measurement-system/`. [Online].

[52] Sebastian Krinner, Simon Storz, Philipp Kurpiers, Paul Magnard, Johannes Heinsoo, Raphael Keller, Janis Luetolf, Christopher Eichler, and Andreas Wallraff. Engineering cryogenic setups for 100-qubit scale superconducting circuit systems. 2018.

[53] Keysight. *Labber User Manual*. Keysight Technologies.

[54] Amr Osman, Jorge Fernández-Pendás, Christopher Warren, Sandoko Kosen, Marco Scigliuzzo, Anton Frisk Kockum, Giovanna Tancredi, Anita Fadavi Roudsari, and Jonas Bylander. Mitigation of frequency collisions in superconducting quantum processors. *Phys. Rev. Res.*, 5:043001, Oct 2023.

[55] Kazi Rafsanjani Amin, Axel M. Eriksson, Mikael Kervinen, Linus Andersson, Robert Rehammar, and Simone Gasparinetti. Direct detection of quasiparticle tunneling with a charge-sensitive superconducting sensor coupled to a waveguide, 2024.

[56] B Foxen, J Y Mutus, E Lucero, E Jeffrey, D Sank, R Barends, K Arya, B Burkett, Yu Chen, Zijun Chen, B Chiaro, A Dunsworth, A Fowler, C Gidney, M Giustina, R Graff, T Huang, J Kelly, P Klimov, A Megrant, O Naaman, M Neeley, C Neill, C Quintana, P Roushan, A Vainsencher, J Wenner, T C White, and John M Martinis. High speed flux sampling for tunable superconducting qubits with an embedded cryogenic transducer. *Superconductor Science and Technology*, 32(1):015012, December 2018.

[57] Youngkyu Sung, Leon Ding, Jochen Braumüller, Antti Vepsäläinen, Bharath Kannan, Morten Kjaergaard, Ami Greene, Gabriel O. Samach, Chris McNally, David Kim, Alexander Melville, Bethany M. Niedzielski, Mollie E. Schwartz, Jonilyn L. Yoder, Terry P. Orlando, Simon Gustavsson, and William D. Oliver. Realization of high-fidelity cz and zz-free iswap gates with a tunable coupler. 2020.

[58] Scipy. scipy.signal.savgol_filter. `https://docs.scipy.org/doc/scipy/reference/generated/scipy.signal.savgol_filter.html`. [Online].

[59] Jürgen Lisenfeld, Alexander Bilmes, Anthony Megrant, Rami Barends, Julian Kelly, Paul Klimov, Georg Weiss, John M. Martinis, and Alexey V. Ustinov. Electric field spectroscopy of material defects in transmon qubits. *npj Quantum Information*, 5(1), November 2019.

[60] Marie Frédérique Dumas, Benjamin Groleau-Paré, Alexander McDonald, Manuel H. Muñoz-Arias, Cristóbal Lledó, Benjamin D'Anjou, and Alexandre Blais. Unified picture of measurement-induced ionization in the transmon, 2024.

[61] Daniel Sank, Zijun Chen, Mostafa Khezri, J. Kelly, R. Barends, B. Campbell, Y. Chen, B. Chiaro, A. Dunsworth, A. Fowler, E. Jeffrey, E. Lucero, A. Megrant, J. Mutus, M. Neeley, C. Neill, P. J. J. O'Malley, C. Quintana, P. Roushan, A. Vainsencher, T. White, J. Wenner, Alexander N. Korotkov, and John M. Martinis. Measurement-induced state transitions in a superconducting qubit: Beyond the rotating wave approximation. *Phys. Rev. Lett.*, 117:190503, Nov 2016.

[62] Jay Gambetta, Alexandre Blais, D. I. Schuster, A. Wallraff, L. Frunzio, J. Majer, M. H. Devoret, S. M. Girvin, and R. J. Schoelkopf. Qubit-photon interactions in a cavity: Measurement-induced dephasing and number splitting. *Physical Review A*, 74(4), October 2006.

[63] D.T. McClure, Hanhee Paik, L.S. Bishop, M. Steffen, Jerry M. Chow, and Jay M. Gambetta. Rapid driven reset of a qubit readout resonator. *Physical Review Applied*, 5(1), January 2016.

[64] Scikit learn. Naive Bayes. `https://scikit-learn.org/stable/modules/naive_bayes.html`. [Online].

[65] Scikit learn. SVC. `https://scikit-learn.org/stable/modules/generated/sklearn.svm.SVC.html`. [Online].

[66] G. Catelani, R. J. Schoelkopf, M. H. Devoret, and L. I. Glazman. Relaxation and frequency shifts induced by quasiparticles in superconducting qubits. *Phys. Rev. B*, 84:064517, Aug 2011.

[67] Wolfgang Eisenmenger, Kurt Lassmann, H. J. Trumpp, and R. Krauß. Quasiparticle recombination and 2δ-phonon-trapping in superconducting tunneling junctions. *Applied physics*, 11:307–320, 1976.

[68] Scipy. scipy.signal.lfilter. `https://docs.scipy.org/doc/scipy/reference/generated/scipy.signal.lfilter.html`. [Online].

[69] Yoni Shalibo, Ya'ara Rofe, David Shwa, Felix Zeides, Matthew Neeley, John M. Martinis, and Nadav Katz. Lifetime and coherence of two-level defects in a josephson junction. *Phys. Rev. Lett.*, 105:177001, Oct 2010.

[70] John M. Martinis, K. B. Cooper, R. McDermott, Matthias Steffen, Markus Ansmann, K. D. Osborn, K. Cicak, Seongshik Oh, D. P. Pappas, R. W. Simmonds, and Clare C. Yu. Decoherence in josephson qubits from dielectric loss. *Physical Review Letters*, 95(21), November 2005.

[71] P. Kumar, S. Sendelbach, M.A. Beck, J.W. Freeland, Zhe Wang, Hui Wang, Clare C. Yu, R.Q. Wu, D.P. Pappas, and R. McDermott. Origin and reduction of 1/f magnetic flux noise in superconducting devices. *Physical Review Applied*, 6(4), October 2016.

[72] F. Yoshihara, K. Harrabi, A. O. Niskanen, Y. Nakamura, and J. S. Tsai. Decoherence of flux qubits due to $1/f$ flux noise. *Phys. Rev. Lett.*, 97:167001, Oct 2006.

[73] M. Mergenthaler, C. Müller, M. Ganzhorn, S. Paredes, P. Müller, G. Salis, V. P. Adiga, M. Brink, M. Sandberg, J. B. Hertzberg, S. Filipp, and A. Fuhrer. Effects of surface treatments on flux tunable transmon qubits. *npj Quantum Information*, 7(1), October 2021.

[74] Y. Yuzhelevski, M. Yuzhelevski, and G. Jung. Random telegraph noise analysis in time domain. *Review of Scientific Instruments*, 71(4):1681–1688, April 2000.

[75] Xianchuang Pan, Yuxuan Zhou, Haolan Yuan, Lifu Nie, Weiwei Wei, Libo Zhang, Jian Li, Song Liu, Zhi Hao Jiang, Gianluigi Catelani, Ling Hu, Fei Yan, and Dapeng Yu. Engineering superconducting qubits to reduce quasiparticles and charge noise. *Nature Communications*, 13(1), November 2022.

[76] R. T. Gordon, C. E. Murray, C. Kurter, M. Sandberg, S. A. Hall, K. Balakrishnan, R. Shelby, B. Wacaser, A. A. Stabile, J. W. Sleight, M. Brink, M. B. Rothwell, K. P. Rodbell, O. Dial, and M. Steffen. Environmental radiation impact on lifetimes and quasiparticle tunneling rates of fixed-frequency transmon qubits. *Applied Physics Letters*, 120(7), February 2022.

[77] O. Rafferty, S. Patel, C. H. Liu, S. Abdullah, C. D. Wilen, D. C. Harrison, and R. McDermott. Spurious antenna modes of the transmon qubit, 2021.

[78] Chuan-Hong Liu, David C. Harrison, Shravan Patel, Christopher D. Wilen, Owen Rafferty, Abigail Shearrow, Andrew Ballard, Vito Iaia, Jaseung Ku, Britton L. T. Plourde, and Robert McDermott. Quasiparticle poisoning of superconducting qubits from resonant absorption of pair-breaking photons, 2022.

[79] Alexander Bilmes, Anthony Megrant, Paul Klimov, Georg Weiss, John M. Martinis, Alexey V. Ustinov, and Jürgen Lisenfeld. Resolving the positions of defects in superconducting quantum bits. *Scientific Reports*, 10(1), February 2020.

[80] Dante Colao Zanuz, Quentin Ficheux, Laurent Michaud, Alexei Orekhov, Kilian Hanke, Alexander Flasby, Mohsen Bahrami Panah, Graham J. Norris, Michael Kerschbaum, Ants Remm, François Swiadek, Christoph Hellings, Stefania Lazăr, Colin Scarato, Nathan Lacroix, Sebastian Krinner, Christopher

Eichler, Andreas Wallraff, and Jean-Claude Besse. Mitigating losses of superconducting qubits strongly coupled to defect modes, 2024.

[81] M. Carroll, S. Rosenblatt, P. Jurcevic, I. Lauer, and A. Kandala. Dynamics of superconducting qubit relaxation times. *npj Quantum Information*, 8(1), November 2022.

[82] Matt McEwen, Kevin C. Miao, Juan Atalaya, Alex Bilmes, Alex Crook, Jenna Bovaird, John Mark Kreikebaum, Nicholas Zobrist, Evan Jeffrey, Bicheng Ying, Andreas Bengtsson, Hung-Shen Chang, Andrew Dunsworth, Julian Kelly, Yaxing Zhang, Ebrahim Forati, Rajeev Acharya, Justin Iveland, Wayne Liu, Seon Kim, Brian Burkett, Anthony Megrant, Yu Chen, Charles Neill, Daniel Sank, Michel Devoret, and Alex Opremcak. Resisting high-energy impact events through gap engineering in superconducting qubit arrays, 2024.

[83] Plamen Kamenov, Thomas DiNapoli, Michael Gershenson, and Srivatsan Chakram. Suppression of quasiparticle poisoning in transmon qubits by gap engineering, 2024.

A

FIR and IIR filter design

After measuring the step response of the flux pulse, we need to convert it to a digital transfer function such that we can correct for it accordingly. The step response we fit to is given by

$$s(t) = \left(1 + a_0 e^{-t/\tau_0} + a_1 e^{-t/\tau_1}\right) \theta(t), \tag{A.1}$$

which has Laplace transform

$$S(s) = \frac{1}{s} + \frac{a_0\tau_0}{1 + s\tau_0} + \frac{a_1\tau_1}{1 + s\tau_1}. \tag{A.2}$$

In Laplace domain, the step response is given by $S(s) = H(s)/s$, so the transfer function is given by $H(s) = sS(s)$, since the Laplace transform of the Heaviside function, $\theta(t)$, is $1/s$. We then find that the transfer function in continuous Laplace space is given by

$$H(s) = S(s)s = \frac{1 + s\left(\tau_0 + a_0\tau_0 + \tau_1 + a_1\tau_1\right) + s^2\left(\tau_0\tau_1 + a_0\tau_0\tau_1 + a_1\tau_0\tau_1\right)}{1 + s\left(\tau_0 + \tau_1\right) + s^2\left(\tau_0\tau_1\right)}, \tag{A.3}$$

which is a second order transfer function. To apply the inverse of this transfer function to our AWG waveform, we need to digitise it, and for that we use the bilinear transform. Writing a general second order transfer function in the continuous Laplace space as

$$H(s) = \frac{b_0 + b_1 s^{-1} + b_2 s^{-2}}{a_0 + a_1 s^{-1} + a_2 s^{-2}}, \tag{A.4}$$

we find that for a second order transformation, applying the bilinear transformation, results in

$$H[z] = \frac{\left(b_0K^2 + b_1K + b_2\right) + \left(2b_2 - 2b_0K^2\right) z^{-1} + \left(b_0K^2 - b_1K + b_2\right) z^{-2}}{\left(a_0K^2 + a_1K + a_2\right) + \left(2a_2 - 2a_0K^2\right) z^{-1} + \left(a_0K^2 - a_1K + a_2\right) z^{-2}}, \tag{A.5}$$

where $K = 2/t_s$, and t_s is the sampling time. This is how an IIR filter is applied, the step response is measured and then converted to a continuous transfer function, for predistortion we apply $1/H(s)$, and then modify the transfer function parameters using the bilinear transformation. These parameters then go into scipy's `lfilter` which applies the digital transfer function to our waveform.

For an FIR filter the situation is a bit different since we do not fit the step response to some function with a number of poles. Instead, we compare our measured result in the time domain, $y[t]$, to our target, $x[t]$, and use a least squares algorithm to find the transfer function parameters, $h[t]$, which, when applied to the output, $y[t]$, best resembles the target $x[t]$.

B

TLS-qubit model: Calculation of the effective qubit decay rate

Our TLS-qubit model is described by the Hamiltonian

$$\begin{aligned} H &= \begin{pmatrix} \omega_{\mathrm{Q}} - i\Gamma_{\mathrm{Q}}/2 & g \\ g & \omega_{\mathrm{TLS}} - i\Gamma_{\mathrm{TLS}}/2 \end{pmatrix} \\ &= \frac{1}{2}\begin{pmatrix} \Delta - i\Gamma_{\mathrm{Q}} & 2g \\ 2g & -\Delta - i\Gamma_{\mathrm{TLS}} \end{pmatrix}. \end{aligned}$$

The perturbation in this model is given by $V = g\sigma_x$, which is an *odd* interaction, so the first order correction to the unperturbed eigenenergies is zero. Using perturbation theory [2], we find that the qubit energy is

$$\begin{aligned} E_{\mathrm{Q}} &= \frac{1}{2}\left(\Delta - i\Gamma_{\mathrm{Q}}\right) + g^2 \frac{|\langle 0|\sigma_x|1\rangle|^2}{\frac{1}{2}\left(2\Delta - i\Gamma_{\mathrm{Q}} + i\Gamma_{\mathrm{TLS}}\right)} \\ &= \frac{1}{2}\left(\Delta - i\Gamma_{\mathrm{Q}}\right) + 2g^2 \frac{1}{2\Delta + i\left(\Gamma_{\mathrm{TLS}} - \Gamma_{\mathrm{Q}}\right)} \\ &= \frac{1}{2}\left(\Delta - i\Gamma_{\mathrm{Q}}\right) + 2g^2 \frac{2\Delta - i\left(\Gamma_{\mathrm{TLS}} - \Gamma_{\mathrm{Q}}\right)}{4\Delta^2 + \left(\Gamma_{\mathrm{TLS}} - \Gamma_{\mathrm{Q}}\right)^2} \\ &= \frac{\Delta}{2} + 2g^2 \frac{2\Delta}{4\Delta^2 + \left(\Gamma_{\mathrm{TLS}} - \Gamma_{\mathrm{Q}}\right)^2} - i\left(\frac{\Gamma_{\mathrm{Q}}}{2} + 2g^2 \frac{\Gamma_{\mathrm{TLS}} - \Gamma_{\mathrm{Q}}}{4\Delta^2 + \left(\Gamma_{\mathrm{TLS}} - \Gamma_{\mathrm{Q}}\right)^2}\right). \end{aligned}$$

Luckily, we find that $\operatorname{Im} E_{\mathrm{Q}}$ is negative, so the qubit indeed has an effective decay rate, the probability of measuring the qubit does not grow in time. Furthermore, we find the effective decay rate, $\Gamma_{\mathrm{eff}} = 2\operatorname{Im} E_{\mathrm{Q}}$, to be

$$\begin{aligned} \Gamma_{\mathrm{eff}} &= \Gamma_{\mathrm{Q}} + 4g^2 \frac{\left(\Gamma_{\mathrm{TLS}} - \Gamma_{\mathrm{Q}}\right)/4}{\Delta^2 + \left(\frac{\Gamma_{\mathrm{TLS}} - \Gamma_{\mathrm{Q}}}{2}\right)^2} \\ &= \frac{2g^2\Gamma}{\Delta^2 + \Gamma^2} + \Gamma_{\mathrm{Q}}, \end{aligned}$$

where $\Gamma = \frac{\Gamma_{\mathrm{TLS}} - \Gamma_{\mathrm{Q}}}{2}$. Also note that perturbation theory is only valid if the perturbation strength is significantly lower than the modulo difference between the two

unperturbed eigenenergies, i.e. when

$$\begin{aligned} g &<< \frac{1}{2}\left|\Delta - i\Gamma_{\mathrm{Q}} + \Delta + i\Gamma_{\mathrm{TLS}}\right| \\ &<< \frac{1}{2}\left|2\Delta + i\left(\Gamma_{\mathrm{TLS}} - \Gamma_{\mathrm{Q}}\right)\right| \\ &<< \frac{1}{2}\sqrt{4\Delta^2 + \left(\Gamma_{\mathrm{TLS}} - \Gamma_{\mathrm{Q}}\right)^2}. \end{aligned}$$

This condition is most restrictive, i.e. the RHS is smallest, on resonance, $\Delta = 0$, where we find $g << \frac{1}{2}\left|\Gamma_{\mathrm{TLS}} - \Gamma_{\mathrm{Q}}\right| = \Gamma$.
I will also take this opportunity to comment on the units of the parameters in our model. The decay rates we measure have units Hz, and this is consistent with our model since a decay rate Γ_t will appear somehow like $e^{-\Gamma_t t}$ leading to a unitless number in the exponent as wanted. The detuning, Δ, appears in the time evolution of states as $e^{i\Delta t}$, so the units of Δ need to be rad/s. Plugging these units into the effective qubit decay rate we find that the units of g are rad/s, not Hz.

C

Single shot calibration and NB classifier

When measuring the qubit parity switches we convert a single IQ measurement into a qubit state. To do this, we need a well calibrated conversion between the two states, to this end we train a Naive Bayes classifier to discriminate between the qubit ground and excited state. In Figure C.1 we show the result of the state training, by plotting the IQ points measured when preparing the qubit in the ground and excited state.

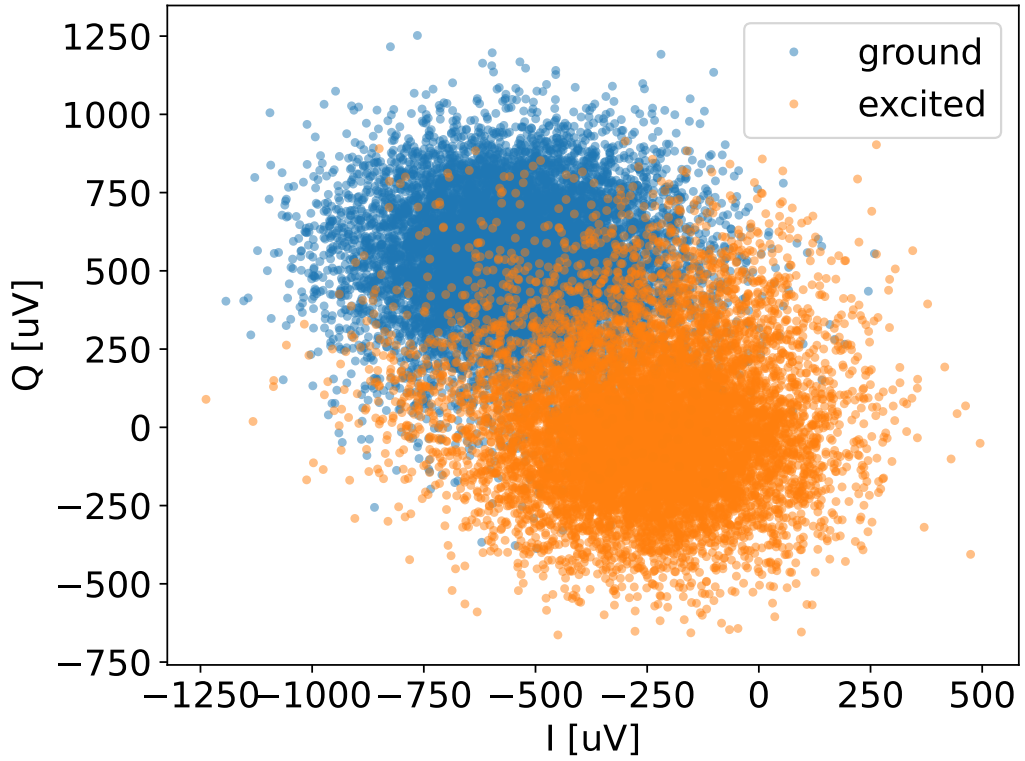

Figure C.1: Qubit state training for single shot measurements. Each state is trained 10k times and fed into a Naive Bayes classifier.

After calibrating both qubit states a Gaussian Naive Bayes (NB) classifier is trained using scikit learn. This also allows us to prepare a test vector, which has prediction accurace of 92%. Note that more single shot fidelity can be reached with higher RO amplitudes, but remember that there is a tradeoff since multiple photons in

the resonator negatively affect the qubit. At higher RO power we also start to see the appearance of higher qubit levels, which we want to avoid in the context of parity switching measurements. We believe there is a sweetspot where the single shot fidelity is just good enough for state discrimination and the RO power is low enough; if the RO power were decreased further then the single shot fidelity would degrade and affect our ability to measure the parity switches.

D

Pulse wrapping: Additional measurements

We performed additional distortions measurements for different flux pulse durations and with different averaging to see how dependent the result was on our measurement. In Figure D.1 we show the result of measuring a millisecond long pulse, where we see that what previously looked similar to an offset is indeed an exponential decay toward the pulse target.

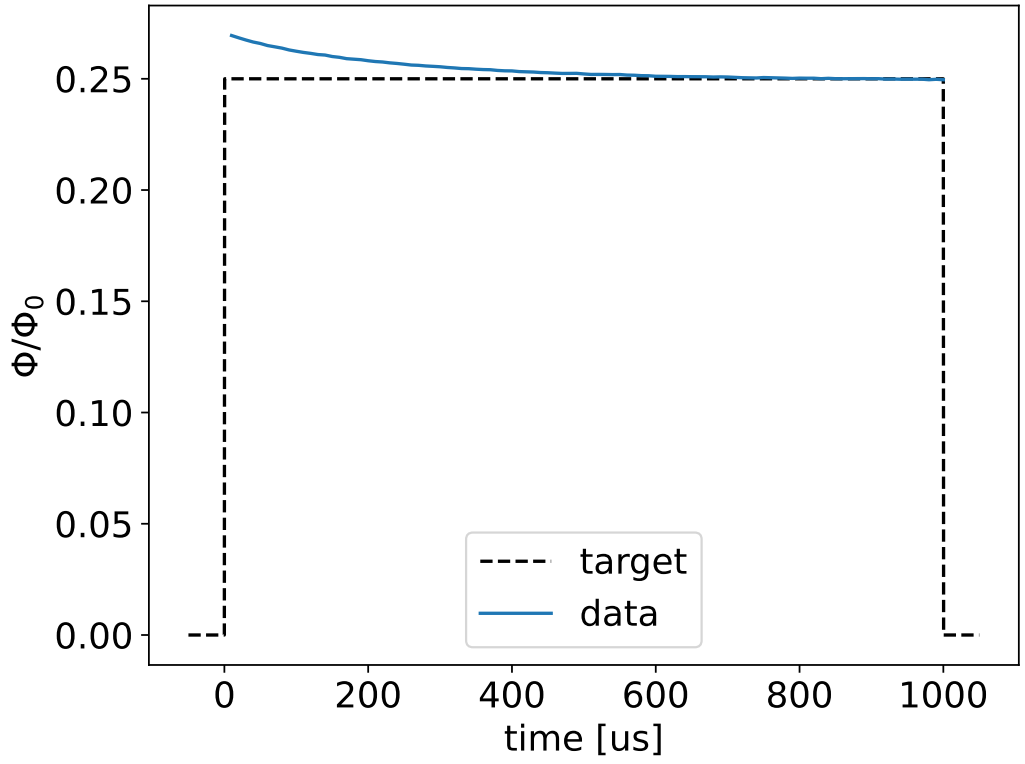

Figure D.1: Pulse wrapping measurement result of a 1 ms long flux pulse. The measured pulse is shown in blue and the target pulse is shown as a dashed black line for reference.

Fitting the step response of Figure D.1 to two exponentials we found a long timescale of $\sim 200\ \mu$s. We did not try to predistort this pulse, measuring it took long enough, and we were only interested in seeing whether there was really an exponential decay toward the target.

We also tried taking more averages and as fine a step size as possible and measured the step response shown in Figure D.2. This measurement took considerable time and was performed to find out whether the distortion parameters extracted with larger sampling time and less averages were viable. The parameters do not vary significantly from the ones presented in Table 4.1.

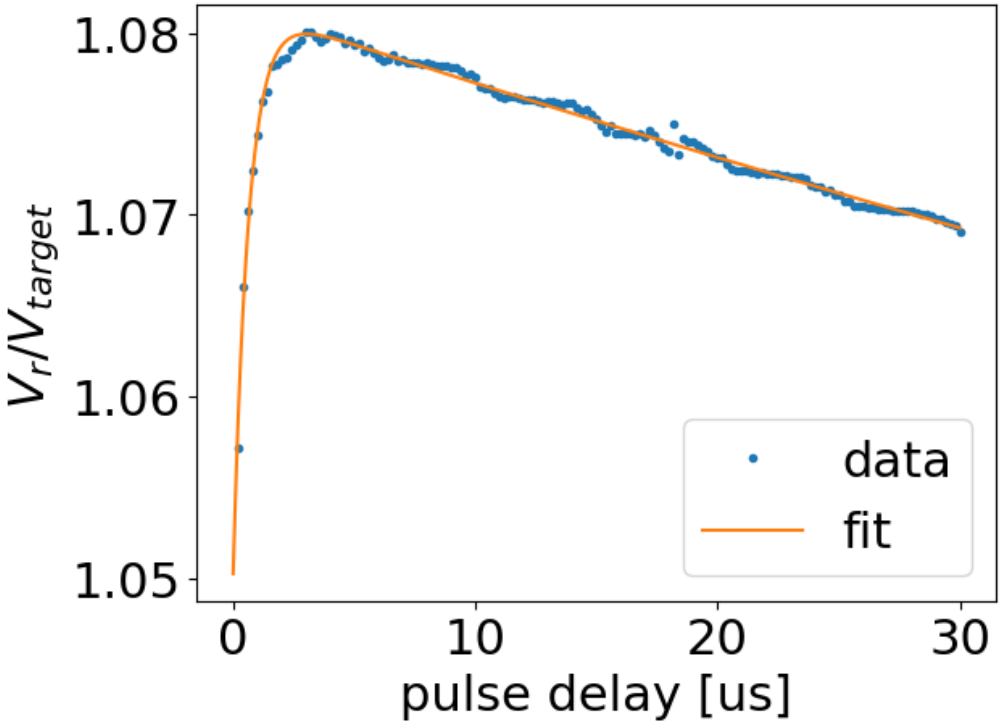

Figure D.2: Pulse wrapping measurement result of a 30 μs flux pulse with 200 ns resolution and 2k averages. The two timescales extracted were 642 ns and 184 μs. Here, the pulse has already been normalised to the target voltage corresponding to 0.25 Φ_0.

E

Room temperature distortion measurements

To investigate the origin of the distortions we measure on the flux pulses we performed a couple of room temperature measurements on pulses of similar shape to the ones used to tune the qubit frequency. In Figure E.1 we show a room temperature digitised square pulse which shows a fast overshoot followed by a small bump. The fast overshoot is LP filtered away when the pulse is sent through the fridge.

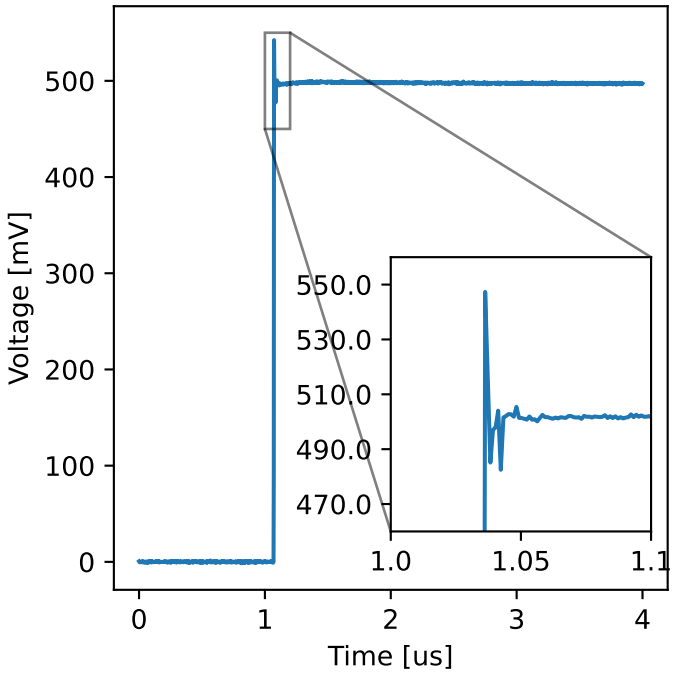

Figure E.1: Room temperature measurement of a 500 mV pulse generated by the AWG and sent straight to the digitiser. There is a fast overshoot followed by some small step response.

Zooming in to see the step response more clearly, shown in Figure E.2, we see a quite familiar shape of the step response. Indeed, it is quite remnant of the distortions we measure through the qubit, as in Subsection 4.1.1. This might indicate that the bulk of the distortion is simply due to the AWG, i.e. some internal electronics of the AWG.
Interestingly, when we send the flux pulse through the fridge at room temperature, we measure the pulse shown in Figure E.3. Now the familiar step response is gone

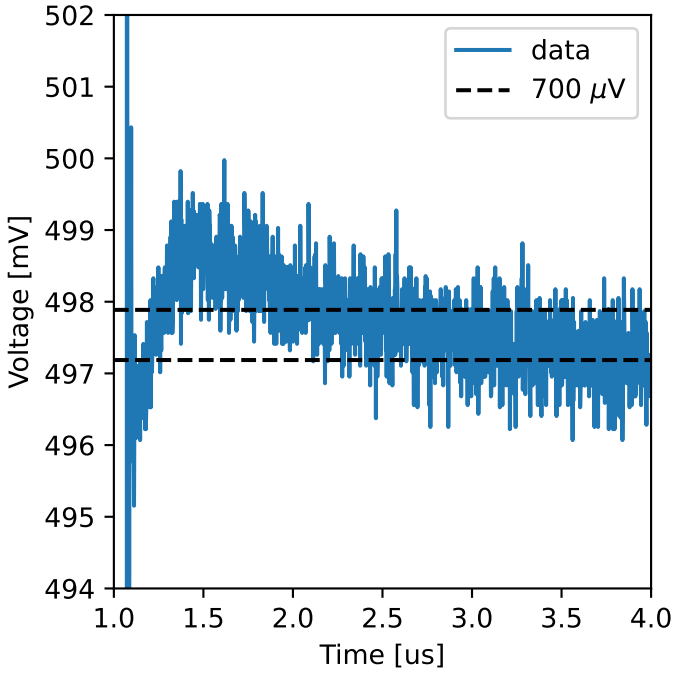

Figure E.2: Zoomed in step response of a 500 mV square pulse sent straight to the digitiser. The shape is similar to what was measured via the qubit. The measured 700 μV noise is both the AWG and digitiser's resolution limit.

and we only measure a slow rise toward the target. The fact that we regain the original pulse shape, which did not travel through the fridge, when we measure the pulse shape in the cold, is unknown. On one hand, there might be some cold effects taking place, such that a pulse travelling through the fridge at room temperature and a pulse travelling through it in the cold experience vastly different distortions. On the other hand, the distortions we measure might be due to the wire bonding on the chip and the flux line, i.e. they could all be from some on-chip effects. Coincidentally, these on-chip effects would lead to the same step response as the AWG initially generates.

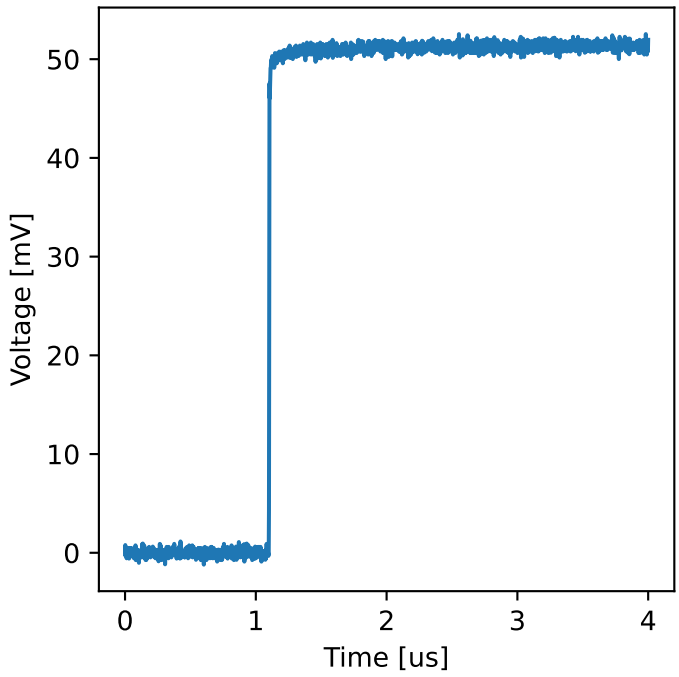

Figure E.3: Measured step response of a square pulse which travelled through the fridge before being digitised. The measured 50 mV amplitude is in correspondence with the 20 dB attenuation on the line.

F

Automatic TLS peak detection and fitting

After performing TLS spectroscopy, we will have a qubit decay rate vs. frequency trace. We assume the qubit decay rate floor to be relatively constant with sharp Lorentzian peaks scattered at different positions. To define the noise floor, we take a histogram of the measured qubit decay rates and fit it to a double exponential, the qubit decay rate with the most counts is defined as `noise_top`. An example of this is shown in Figure F.1, where the data, fit and extracted `noise_top` is shown, along with a kind of FWHM. The qubit decay rate at the FWHM above the rate corresponding to the `noise_top` is referred to as `rate_by_2`.

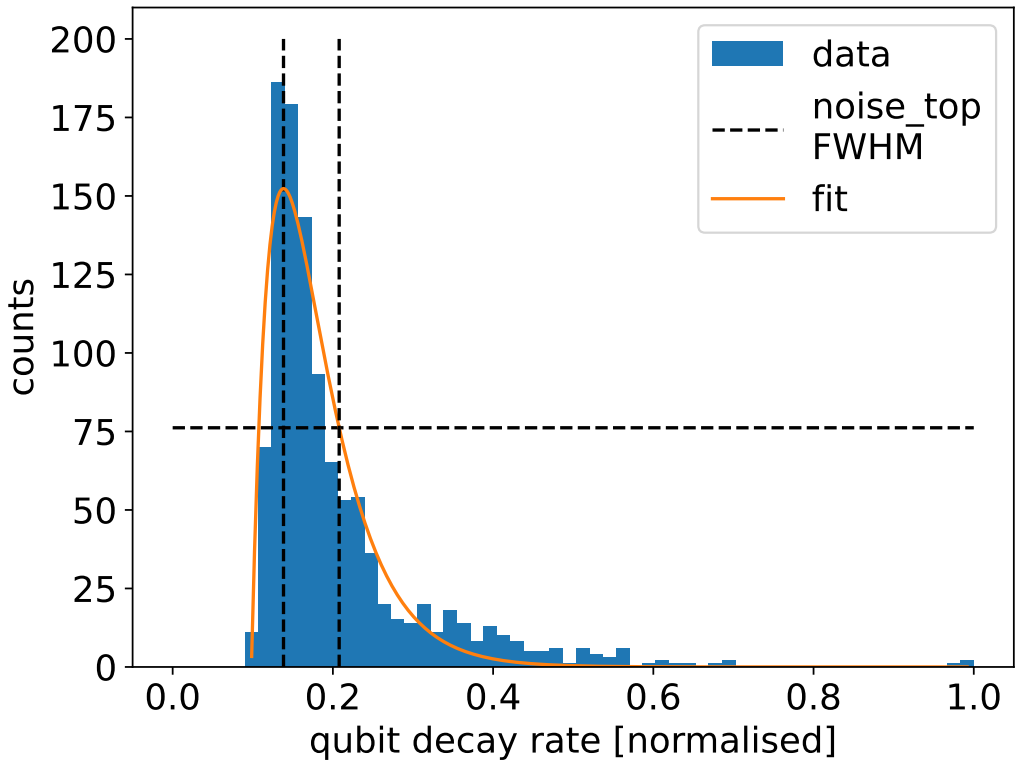

Figure F.1: Histogram of the qubit decay rate measured in a TLS spectroscopy experiment. The histogram is fit to a double exponential whose peak is defined as the noise top, and is used in the automatic peak detection and fitting script.

To find the initial peaks we use `scipy`'s `signal.find_peaks`, with the most im-

portant parameters being `height` and `prominence`. For the results here, `height` was set to `rate_by_2`, and `prominence` was set to `noise_top`. It is not guaranteed that these are optimal parameters but they seemed versatile enough for our results. The automatic fitting script finds a subregion of the whole trace to which for each TLS peak, which a Lorentzian is fit to. This was done by placing ourselves at the top of a TLS peak and walking in each direction until the FWHM of the peak was reached. The frequency which we walked over is chosen as our initial guess for the TLS Lorentzian width. To find the subregion for fitting, we kept walking until `rate_by_2` was reached, the datapoints which we walked over were then used for fitting to a Lorentzian. In Figure F.2 we show an example of the fitting result, where Lorentzians with poor fits have already been removed. The solid green lines show the fit.

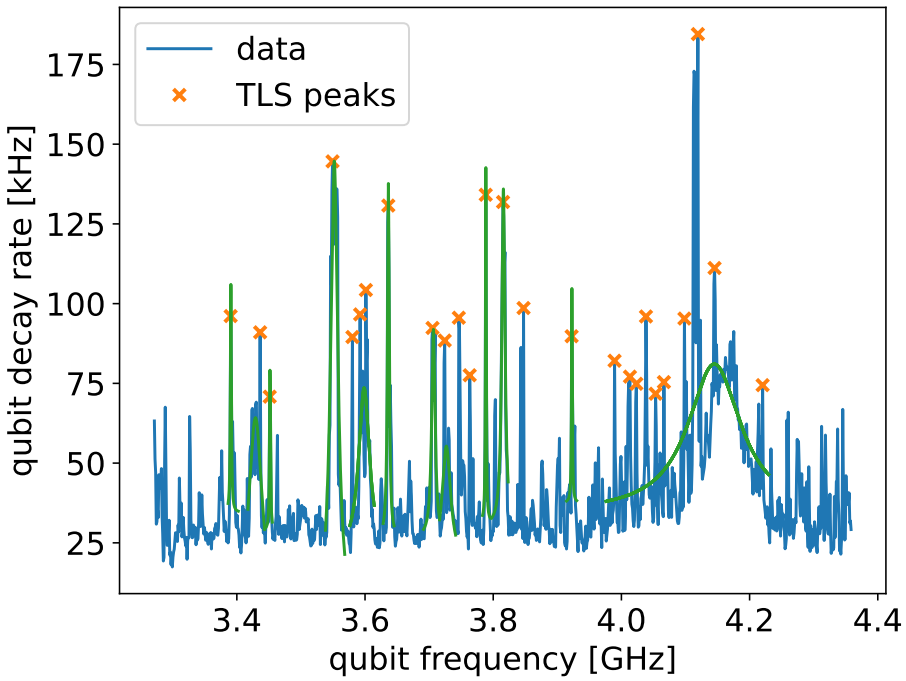

Figure F.2: The green solid lines show the resulting Lorentzian fits of each TLS peak. The poor fits are thrown away and not drawn on this plot. We show how a wide TLS peak can prevent sharper TLS peaks from being detected by the automatic fitting script.

This peak detection and fitting is not perfect. Too many TLS peaks that look reasonable are unable to be fit to. It is also difficult to accurately fit to wide Lorentzians, especially if there are sharp TLSs on top of the wide TLS. As is, the script can either fit to the sharp Lorentzians on top, or ignore them and fit to the wide TLS, so there appears to be a tradeoff in which kind of TLSs we are interested in. It is also very common to have TLSs close to each other, which might be a manifestation of how slow it takes to collect the trace, perhaps the TLS is switching between the two frequencies measured. To prevent double counting TLSs, there is an additional check which makes sure the fitted TLSs are at least 1 MHz apart.

DEPARTMENT OF MICROTECHNOLOGY AND NANOSCIENCE
CHALMERS UNIVERSITY OF TECHNOLOGY
Gothenburg, Sweden
www.chalmers.se

CHALMERS
UNIVERSITY OF TECHNOLOGY